PROCEEDINGS A

royalsocietypublishing.org/journal/rspa

Research

Cite this article: Suleman K, Bosi F. 2022 Direct stress computations in arbitrarily shaped thin shells and elliptic bulge tests. *Proc. R. Soc. A* **478**: 20220619. https://doi.org/10.1098/rspa.2022.0619

Received: 23 September 2022
Accepted: 1 November 2022

Subject Areas:
mechanics, mechanical engineering, mathematical modelling

Keywords:
finite difference method, thin shell, bulge test, parameter identification, digital image correlation

Author for correspondence:
Federico Bosi
e-mail: f.bosi@ucl.ac.uk

Downloaded from https://royalsocietypublishing.org/ on 14 December 2022

Direct stress computations in arbitrarily shaped thin shells and elliptic bulge tests

Khurram Suleman and Federico Bosi

Department of Mechanical Engineering, University College London, London WC1E 6BT, UK

FB, 0000-0002-3638-5307

Most of engineering and biological thin shell structures are characterized by non-axisymmetric and statically indeterminate configurations, which often require the knowledge of the constitutive material model to determine the stress state. In this work, a forward elastostatic method is introduced for the direct stress measurements in elastic homogeneous thin shells of arbitrary shape. The stress distribution is proven to be independent of the material properties for incompressible solids, while in compressible materials it depends only on the Poisson's ratio, which is shown to have a negligible influence on the stress state. Hence, the proposed technique enables the direct assessment of the stress field in statically indeterminate thin shells without a known material model. The shell formulation is implemented using the finite difference method to independently measure the stresses during finite inflation of planar elliptical membranes and from the deformed shapes obtained through digital image correlation during bulge tests on a hyperelastic material, showing very good agreement with finite-element predictions and the applicability of the method to nonlinear elastic materials. Therefore, the procedure can be coupled with imaging techniques for the direct assessment of stresses in thin shell structures and in the identification of material parameters through non-axisymmetric bulge tests.

© 2022 The Authors. Published by the Royal Society under the terms of the Creative Commons Attribution License http://creativecommons.org/licenses/by/4.0/, which permits unrestricted use, provided the original author and source are credited.

THE ROYAL SOCIETY PUBLISHING

Downloaded from https://royalsocietypublishing.org/ on 14 December 2022

1. Introduction

Thin shells are one of the most widely used structural elements in civil [1], mechanical [2,3], architectural [4], biomedical [5,6], aeronautical [7] and aerospace [8,9] applications because they enable complex and large shapes while maintaining minimal weight. The limited thickness requires a careful characterization and modelling of the behaviour of shell structures, to thoroughly assess the stress distribution and avoid structural failure [10–13]. Although the stresses in statically determinate thin shell configurations can be analytically obtained from equilibrium equations in most of the cases [14], complex non-axisymmetric and statically indeterminate shapes require numerical analyses that necessitate the material constitutive model for an accurate prediction of the mechanical behaviour. However, oftentimes the material response is not known beforehand and needs to be identified along with its parameters through direct or iterative inverse method [15–17], thus hindering the prediction of the stress distribution in statically indeterminate shells. This situation occurs in the *in vivo* determination of the stress resultants in non-axisymmetric biological membranes [5,18], in the stress monitoring of civil and mechanical shell structures [1] and in bulge (also known as diaphragm or inflation) tests, an experimental procedure used to characterize the biaxial response and identify the material parameters through the inflation of planar membranes or thin shells subjected to a uniform pressure [19–21]. In these applications, the stress determination relies on the full-field assessment of the deformed configuration through digital image correlation [22,23].

In bulge experiments, the mechanical characterization of thin films is commonly performed by measuring the stress and strain fields independently at the apex of the inflated sample, even though additional multiaxial data can be obtained from the entire shell surface [24]. Diaphragm tests have been widely used with both axisymmetric samples, such as circular [21,25,26] and non-axisymmetric shapes, including square and rectangular [27–30]. Once inflated, the circular and square isotropic shells result in an equibiaxial stress state at the apex, whereas rectangular membranes show different ratios of the principal stresses at their centre. The inflation of the non-axisymmetric membranes has also been extended to elliptical profiles to avoid failure occurring at the edges [31]. For the inflation of circular membranes, analytical solutions have been developed to directly obtain the stress measurements using axisymmetric equilibrium equations on a deformed configuration, without requiring any constitutive relations [32,33]. However, due to the independence of principal curvatures in statically indeterminate and non-axisymmetric shapes, a closed-form expression for the stresses cannot be obtained, and if the material constitutive behaviour is unknown, only approximations exist for some geometries, which undermine the accuracy of the solution. Hence, most of the existing formulations to determine the stresses in statically indeterminate shells rely on the constitutive relations while using the deformation history. Such a procedure cannot be employed in non-axisymmetric bulge experiments for inverse problems, where the material parameters should be identified through the test, nor in the direct stress determination of statically indeterminate shell structures when a precise material model is not known. Therefore, the aim of this work is to develop an accurate method to directly determine the stress distribution in thin shells of arbitrary shape without requiring the material constitutive relation and using only the current deformed configuration, experimentally obtainable through optical techniques, along with its boundary and loading conditions.

Within this framework, Vlassak & Nix [34] developed a method that requires the full deformation history to obtain the material properties and residual stress through square and rectangular bulge tests, assuming Hookean material and small deformations. Their technique was used later to determine the mechanical properties of 3C-SiC membranes [27], TiN [28] and silicon nitride [29] thin films. Neggers *et al.* [35] and Kalkman *et al.* [30] worked on the inflation of rectangular membranes to find the stress at the apex using plane strain approximation for aspect ratios greater than 4. Khayat & Derdouri [36,37] studied the free and confined inflation of arbitrarily shaped and cylindrical hyperelastic membranes for blow moulding applications. The bulging of planar elliptical membranes was studied by Verron *et al.* [38] using a dynamic finite-element analysis (FEA) and explicit finite difference method (FDM), assuming hyperelastic

Downloaded from https://royalsocietypublishing.org/ on 14 December 2022

and viscoelastic material models, respectively. Jayyosi *et al.* [39] analysed the accuracy in fitting an ellipsoid to the inflated shape of an initially planar elliptical membrane of 1, 2 and 4 aspect ratios; they found small shape deviation, which can lead to pronounced errors in the stress or strain determination. Tonge *et al.* [40,41] approximated the deformed cross sections along the planes of symmetry through ellipses. They calculated the stresses at the apex of the deformed shape by using equilibrium expressions from axisymmetric theory, which showed reasonable agreement with FEA but cannot be generalized to any arbitrary shape. Similarly, Yousif *et al.* [31] modelled the bulging of elliptical diaphragms by approximating the deformed section in the major axis with a circular profile, which produces a significant discrepancy in the stress and strain measures.

Lastly, the finite-element inverse elastostatic method has been applied to arbitrarily shaped biological membranes and shells made of incompressible hyperelastic materials [5,18]. The technique considers the known deformed shape and loading conditions, and works backwards to find the initial unstressed configuration along with the stresses in the deformed state [42]. However, the non-uniqueness of the obtained stress-free configuration, which relies on accurate knowledge of the material response, represents a limitation of the procedure. By contrast, the thin shell formulation conceals the opportunity to perform a forward linear analysis on statically indeterminate spatial configurations in order to directly obtain the corresponding stress state, in equilibrium with the known external loads. By considering the deformed shape as the reference configuration, a forward linear analysis could provide the current stress distribution under virtual strains and displacements.

Therefore, this work introduces a forward elastostatic method for the direct stress determination in homogeneous thin shells of arbitrary shape subjected to uniform pressure and undergoing finite deformation, in the absence of a known material constitutive model. The linear elastostatic shell formulation is presented in §2, starting from the description of the geometry of the shell middle surface in §2a, which is followed by the governing equations in §2b. The procedure is numerically implemented through a finite difference code and applied to the stress measurement during the bulging of elliptical thin shells in §2c. It is shown that, if the shell spatial configuration and applied pressure are known, the stress measurement results independent of the material properties for incompressible materials, and only depends on Poisson's ratio for compressible solids. The validation of the proposed technique is presented and discussed in §3, which reports a comparison with FE analyses and the assessment of the influence of an unknown Poisson's ratio on the stress distribution (§3a). Furthermore, the presented formulation is applied to the direct stress calculation during diaphragm inflation experiments on a hyperelastic material, proving its applicability to nonlinear elastic solids (§3b).

2. Stress determination in arbitrarily shaped shells through forward elastostatic analysis

The determination of stresses, strains and displacements in statically indeterminate shell structures often relies on the assumption of small displacements through a linear shell formulation that involves a combination of equilibrium, constitutive model and compatibility equations. When the stress state is sought in a statically indeterminate deformed thin shell configuration, but the material constitutive model is unknown, an analogy can be set between a soft shell undergoing finite deformation until a certain spatial configuration and a stiff shell of identical shape, considered its reference state, subjected to the same loading and boundary conditions. The equilibrium equations in the known configuration, and therefore the stress distribution, remain the same. This observation will be used in the following elastostatic formulation to obtain the stresses in any known non-axisymmetric shell configurations, independently of the previous deformation history.

In the development of a method for the direct stress determination in shells of arbitrary shapes made of a homogeneous elastic material, the choice of the coordinate system can help to minimize the complexity of the formulation and its solution. Therefore, the two principal curvatures of

Downloaded from https://royalsocietypublishing.org/ on 14 December 2022

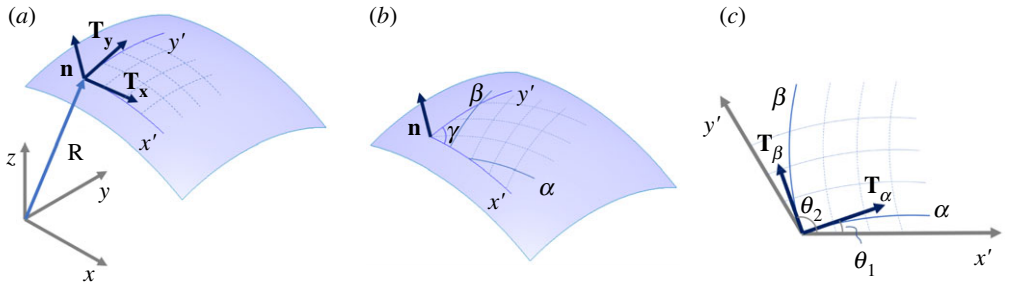

Figure 1. (*a*) Three-dimensional view of the middle surface of an infinitesimal element taken from a deformed shell, where the geometry of the surface is defined by position vector **R** in Cartesian coordinates *xyz*. Normal vector **n** and tangent vectors $\mathbf{T_x}$ and $\mathbf{T_y}$, aligned with the curvilinear local coordinate system $x'y'$, are also shown. (*b*) Element of the middle surface showing curvilinear coordinates $x'y'$ and principal curvature coordinates $\alpha\beta$. (*c*) Lines of principal curvature $\alpha\beta$ mapped on a local tangent plane formed by $x'y'$, where the tangent vectors $\mathbf{T}_\alpha$ and $\mathbf{T}_\beta$ make angle θ_1 and θ_2 with the x' axis, respectively. (Online version in colour.)

the shell surface will be employed as a local orthogonal coordinate system. Since the spatial configuration of the shells is usually given in global coordinates, the transformation from a global coordinate system to local principal coordinates (and vice-versa) is required. Hence, in the following subsection, the geometry of the middle surface of a thin shell is considered to develop the relations that will be used later in §2b to transform between global and local coordinate systems and implement the formulation for the direct stress determination in inflated elliptical shells (§2c).

(a) Geometry of the middle surface of an arbitrarily shaped shell

An element taken from the surface of a shell of arbitrary shape, figure 1*a*, can be represented in global Cartesian coordinates as $z = f(x, y)$. The position vector of a point on the surface takes the form $\mathbf{R} = [x, y, z(x, y)]$, where bold symbols are used to denote vectors throughout this paper. A local curvilinear coordinate system, $x'y'$, can be formed by projecting x and y axes on the shell surface. The coordinates system $x'y'$ is not necessarily orthogonal and is characterized by the angle γ between x' and y', figure 1*b*. The tangents to the curves x' and y' at each point of the surface are given by the vectors $\mathbf{T_x} = [1, 0, \partial z/\partial x]$ and $\mathbf{T_y} = [0, 1, \partial z/\partial y]$, respectively, which form the base vectors of the local coordinate system $x'y'$. The normal unit vector $\mathbf{n}$ is obtained by the cross product of the two tangent vectors as $\mathbf{n} = \mathbf{T_x} \times \mathbf{T_y}/|\mathbf{T_x} \times \mathbf{T_y}|$.

The shell surface can be fully characterized by curvature and metric tensors [43]. A curvature tensor carries the information on the local shape changes of the surface, whereas a metric tensor is related to the local coordinate system of a surface. The components of the curvature tensor in local coordinates $x'y'$ are given by Green & Zerna [44]

$$b_{xx} = \mathbf{n} \cdot \frac{\partial \mathbf{T_x}}{\partial x}, \quad b_{yy} = \mathbf{n} \cdot \frac{\partial \mathbf{T_y}}{\partial y}, \quad b_{xy} = \mathbf{n} \cdot \frac{\partial \mathbf{T_x}}{\partial y} = \mathbf{n} \cdot \frac{\partial \mathbf{T_y}}{\partial x}, \tag{2.1}$$

while the components of the metric tensor in the same coordinates are

$$T_{xx} = \mathbf{T_x} \cdot \mathbf{T_x}, \quad T_{yy} = \mathbf{T_y} \cdot \mathbf{T_y}, \quad T_{xy} = \mathbf{T_x} \cdot \mathbf{T_y}. \tag{2.2}$$

The metric tensor is an important feature of a curvilinear coordinate system to parametrically describe the lengths of the coordinate base vectors and the angles between them. For example, denoting an infinitesimal segment of the curve x' by dx', $dx' = \sqrt{T_{xx}}\, dx$. It can be seen from equations (2.1) and (2.2) that the non-diagonal terms of the curvature and metric tensors, b_{xy} and T_{xy}, are non-zero, thus indicating non-principal coordinates and non-orthogonality of $x'y'$

Downloaded from https://royalsocietypublishing.org/ on 14 December 2022

coordinate system, which leads to complex mathematical expressions for kinetic and kinematic relations.

Hence, in order to simplify the subsequent shell formulation, a new orthogonal coordinate system $\alpha\beta$ can be introduced, figure 1*b*, formed by the lines of principal curvature of the surface. The curvature and metric tensors can also be defined in $\alpha\beta$ coordinates as a function of the base vectors, $\mathbf{T}_\alpha$ and $\mathbf{T}_\beta$, which are tangents to the α and β curves, respectively. The vectors $\mathbf{T}_\alpha$ and $\mathbf{T}_\beta$ can be written as the derivatives of the position vector $\mathbf{R}$ with respect to α and β,

$$\mathbf{T}_\alpha = \left[\frac{\partial x}{\partial \alpha}, \frac{\partial y}{\partial \alpha}, \frac{\partial z}{\partial \alpha}\right] \quad \text{and} \quad \mathbf{T}_\beta = \left[\frac{\partial x}{\partial \beta}, \frac{\partial y}{\partial \beta}, \frac{\partial z}{\partial \beta}\right]. \tag{2.3}$$

The partial derivatives in equation (2.3) are not known beforehand, as the relation between the principal coordinates $\alpha\beta$ and the global coordinates xyz is unknown for an arbitrary shape of the surface. Therefore, $\mathbf{T}_\alpha$ and $\mathbf{T}_\beta$ are found by rotating $\mathbf{T}_\mathbf{x}$ by the angles θ_1 and θ_2 that the principal curves α and β make with $\mathbf{T}_\mathbf{x}$, respectively, figure 1*c*. These angles can be determined from the slopes $\lambda_{1,2}$ of the tangents of α and β curves in the local coordinate system $x'y'$ [45]

$$\lambda_{1,2} = \frac{-(b_{xx}T_{yy} - b_{yy}T_{xx}) \pm \sqrt{(b_{xx}T_{yy} - b_{yy}T_{xx})^2 - 4(b_{xy}T_{yy} - b_{yy}T_{xy})(b_{xx}T_{xy} - b_{xy}T_{xx})}}{2(b_{xy}T_{yy} - b_{yy}T_{xy})}. \tag{2.4}$$

Equation (2.4) is a result of a quadratic equation obtained by imposing $\mathrm{d}\kappa_n/\mathrm{d}\lambda_{1,2} = 0$, where κ_n is the normal curvature of the surface [45]. From the trigonometry of figure 1*c*, the angles θ_1 and θ_2 can be written as

$$\theta_{1,2} = \arctan\left[\frac{\lambda_{1,2}\ \sin(\pi - \gamma)}{1 - \lambda_{1,2}\ \cos(\pi - \gamma)}\right]. \tag{2.5}$$

The tangent vectors, $\mathbf{T}_\alpha$ and $\mathbf{T}_\beta$, can now be written as the rotation of $\mathbf{T}_\mathbf{x}$ by θ_1 and θ_2 about the normal vector $\mathbf{n}$ [46]

$$\begin{aligned} &\mathbf{T}_\alpha = \mathbf{T}_\mathbf{x}\cos\theta_1 + \mathbf{n}(\mathbf{n}\cdot\mathbf{T}_\mathbf{x})(1-\cos\theta_1) + (\mathbf{T}_\mathbf{x}\times\mathbf{n})\sin\theta_1 \\ \text{and} \quad &\mathbf{T}_\beta = \mathbf{T}_\mathbf{x}\cos\theta_2 + \mathbf{n}(\mathbf{n}\cdot\mathbf{T}_\mathbf{x})(1-\cos\theta_2) + (\mathbf{T}_\mathbf{x}\times\mathbf{n})\sin\theta_2. \end{aligned} \tag{2.6}$$

Equations (2.6) and (2.3) are useful to transform xy coordinates to the $\alpha\beta$ coordinate system by comparing their right-hand sides and using the chain rule, as will be shown in the following. After obtaining the base vectors $\mathbf{T}_\alpha$ and $\mathbf{T}_\beta$ for principal coordinates, the curvature and metric tensorial components can be written as

$$b_{\alpha\alpha} = \mathbf{n}\cdot\frac{\partial \mathbf{T}_\alpha}{\partial \alpha}, \quad b_{\beta\beta} = \mathbf{n}\cdot\frac{\partial \mathbf{T}_\beta}{\partial \beta}, \quad b_{\alpha\beta} = \mathbf{n}\cdot\frac{\partial \mathbf{T}_\alpha}{\partial \beta} = \mathbf{n}\cdot\frac{\partial \mathbf{T}_\beta}{\partial \alpha} = 0, \tag{2.7}$$

and

$$T_{\alpha\alpha} = \mathbf{T}_\alpha\cdot\mathbf{T}_\alpha, \quad T_{\beta\beta} = \mathbf{T}_\beta\cdot\mathbf{T}_\beta, \quad T_{\alpha\beta} = \mathbf{T}_\alpha\cdot\mathbf{T}_\beta = 0. \tag{2.8}$$

It should be noted that the diagonal terms of the curvature and metric tensors in equations (2.7) and (2.8) are null, since $\alpha\beta$ is an orthogonal principal coordinate system. Since $\mathbf{T}_\alpha$ and $\mathbf{T}_\beta$ are functions of x and y, the partial derivative terms in equation (2.7) can be expanded using the chain rule. For instance, $\partial\mathbf{T}_\alpha/\partial\alpha$ takes the form

$$\frac{\partial \mathbf{T}_\alpha}{\partial \alpha} = \frac{\partial \mathbf{T}_\alpha}{\partial x}\frac{\partial x}{\partial \alpha} + \frac{\partial \mathbf{T}_\alpha}{\partial y}\frac{\partial y}{\partial \alpha}. \tag{2.9}$$

The partial derivatives $\partial x/\partial\alpha$ and $\partial y/\partial\alpha$ can be obtained by comparing equation (2.6) with equation (2.3). Similarly, the expression for $\mathbf{T}_\beta/\partial\beta$ can be found. Furthermore, the surface can

Downloaded from https://royalsocietypublishing.org/ on 14 December 2022

also be characterized by Lame's coefficients [45], denoted by A and B, which are the square root of the components of the metric tensor

$$A = \sqrt{T_{\alpha\alpha}} \quad \text{and} \quad B = \sqrt{T_{\beta\beta}}. \tag{2.10}$$

The Lame's coefficients will be used to express the equilibrium and compatibility equations for the shell formulation reported in the next section. Lastly, the radii of principal curvatures R_1 and R_2, corresponding to α and β curves, respectively, are given by

$$R_1 = \frac{T_{\alpha\alpha}}{b_{\alpha\alpha}} \quad \text{and} \quad R_2 = \frac{T_{\beta\beta}}{b_{\beta\beta}}. \tag{2.11}$$

For curvilinear coordinates, the radius of curvature cannot be given as the reciprocal of the component of the curvature tensor. Instead, it should be multiplied with the respective component of the metric tensor since the base vectors are not necessarily the unit vectors, as it occurs for Cartesian coordinates. The above relations for the shell middle surface will be used in the following sections to present the governing equations for thin shells and transform them from principal to Cartesian coordinates.

(b) Governing equations

A thin shell is clamped at its edge and subjected to a uniform normal pressure p, in static equilibrium, as shown in figure 2*a*. It should be noted that, although the figure shows an elliptic paraboloid-like non-axisymmetric configuration, the governing equations presented in this section are valid for any arbitrarily shaped thin shell. For a known equilibrium configuration, using principal curvature coordinates $\alpha\beta$, the local equilibrium is represented by a linear system given by Ventsel & Krauthammer [45]

$$\begin{aligned}
&\frac{\partial}{\partial\alpha}(N_1 B) + \frac{1}{A}\frac{\partial}{\partial\beta}(SA^2) - \frac{2H}{R_2}\frac{\partial A}{\partial\beta} \\
&\qquad - \frac{1}{R_1}\left(\frac{\partial}{\partial\alpha}(M_1 B) - M_2\frac{\partial B}{\partial\alpha} + 2\frac{\partial}{\partial\beta}(HA)\right) - N_2\frac{\partial B}{\partial\alpha} = 0 \\
&\frac{\partial}{\partial\beta}(N_2 A) + \frac{1}{B}\frac{\partial}{\partial\alpha}(SB^2) - \frac{2H}{R_1}\frac{\partial B}{\partial\alpha} \\
&\qquad - \frac{1}{R_2}\left(\frac{\partial}{\partial\beta}(M_2 A) - M_1\frac{\partial A}{\partial\beta} + 2\frac{\partial}{\partial\alpha}(HB)\right) - N_1\frac{\partial A}{\partial\beta} = 0
\end{aligned} \tag{2.12}$$

and

$$\begin{aligned}
&N_1\frac{AB}{R_1} + N_2\frac{AB}{R_2} + \frac{\partial}{\partial\alpha}\left\{\frac{1}{A}\left[\frac{1}{A}\frac{\partial}{\partial\beta}(A^2H) + \frac{\partial}{\partial\alpha}(BM_1) - M_2\frac{\partial B}{\partial\alpha}\right]\right\} \\
&\quad + \frac{\partial}{\partial\beta}\left\{\frac{1}{B}\left[\frac{1}{B}\frac{\partial}{\partial\alpha}(B^2H) + \frac{\partial}{\partial\beta}(AM_2) - M_1\frac{\partial A}{\partial\beta}\right]\right\} + ABp = 0,
\end{aligned}$$

where $S = N_{12} + H/R_2 = N_{21} + H/R_1$, N_i $(i = 1, 2)$ represents the normal stress resultants (force per unit width), N_{12} or N_{21} denote the in-plane shear stress resultants, figure 2*b*, M_i $(i = 1, 2)$ and H are the bending and twisting moments per unit width, figure 2*c*, while the subscripts $i = 1$ and $i = 2$ denote the principal curvature directions α and β, respectively. The stress resultants and moments used in the equilibrium equations are expressed in terms of stresses in appendix A, while the coefficients R_1, R_2, A and B are functions of the known geometry of the shell, equations (2.10) and (2.11). If the boundary conditions are in the form of imposed stress resultants and moments, equation (2.12) is sufficient to obtain the stresses over the entire shell. However, a thin shell with prescribed displacements, such as clamped edges, represents a statically indeterminate problem for which kinematics need to be used [47,48]. In both cases of a thin shell having an initial configuration as shown in figure 2*a* and undergoing small deformation, or a thin shell reaching

Downloaded from https://royalsocietypublishing.org/ on 14 December 2022

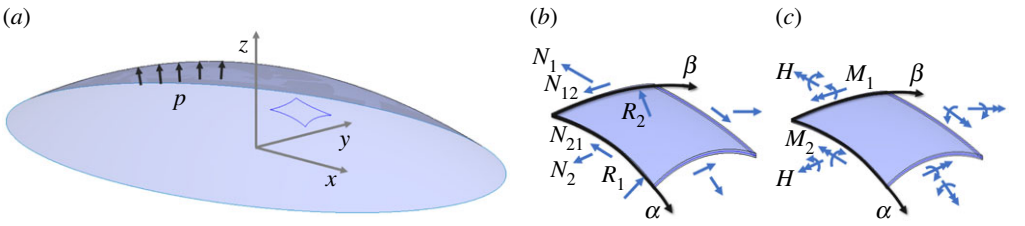

Figure 2. (*a*) Geometry of a clamped thin shell subjected to a normal pressure p, and an element of the shell showing force (*b*) and moment (*c*) resultants in principal coordinates $\alpha\beta$. (Online version in colour.)

the same state after finite deformation, if the pressure p and boundary conditions are identical, the equilibrium equations and the stress distribution remain the same. This analogy will be employed to obtain the stresses in statically indeterminate thin shells through a forward linear analysis of the three-dimensional equilibrium configuration, irrespective of the previous deformation history. Therefore, the elastic constitutive relations for a general homogeneous isotropic material undergoing small deformation are given by

$$N_1 = \frac{Eh}{1-\nu^2}(\varepsilon_1 + \nu\varepsilon_2), \quad N_2 = \frac{Eh}{1-\nu^2}(\nu\varepsilon_1 + \varepsilon_2), \quad S = \frac{Eh}{2(\nu+1)}\gamma_{12}$$
$$\text{and} \qquad M_1 = \frac{Eh^3}{12(1-\nu^2)}(\chi_1 + \nu\chi_2), \quad M_2 = \frac{Eh^3}{12(1-\nu^2)}(\nu\chi_1 + \chi_2), \quad H = \frac{Eh^3}{12(\nu+1)}\chi_{12}, \tag{2.13}$$

where ε_i $(i=1,2)$ are the normal strains for the middle surface, γ_{12} is the in-plane shear, χ_i $(i=1,2,12)$ denote the change in curvatures, E is Young's modulus, ν is the Poisson's ratio and h is the thickness of the shell in the reference configuration, figure 2, which remains small compared with the shell radii of curvature. Although the constitutive relations are written here for a linear elastic material, it will be shown in the following sections that the stresses result independent of the material parameters and of the Young's modulus E, for incompressible and compressible solids, respectively. Therefore, the formulation can be employed for other linearized constitutive relations. This observation is fundamental for the development of a forward elastostatic procedure to directly obtain the stress distribution in statically indeterminate non-axisymmetric shells, without requiring the knowledge of the material model. Denoting the displacements u, v and w along the α, β and normal directions of the equilibrium configuration of the shell, the strain–displacement relations are given by Ventsel & Krauthammer [45]

$$\varepsilon_1 = \frac{1}{A}\frac{\partial u}{\partial \alpha} + \frac{1}{AB}\frac{\partial A}{\partial \beta}v - \frac{w}{R_1}$$
$$\varepsilon_2 = \frac{1}{B}\frac{\partial v}{\partial \beta} + \frac{1}{AB}\frac{\partial B}{\partial \alpha}u - \frac{w}{R_2}$$
$$\gamma_{12} = \frac{B}{A}\frac{\partial}{\partial \alpha}\left(\frac{v}{B}\right) + \frac{A}{B}\frac{\partial}{\partial \beta}\left(\frac{u}{A}\right)$$
$$\chi_1 = -\frac{1}{A}\frac{\partial}{\partial \alpha}\left(\frac{u}{R_1} + \frac{1}{A}\frac{\partial w}{\partial \alpha}\right) - \frac{1}{AB}\frac{\partial A}{\partial \beta}\left(\frac{v}{R_2} + \frac{1}{B}\frac{\partial w}{\partial \beta}\right) \tag{2.14}$$
$$\chi_2 = -\frac{1}{B}\frac{\partial}{\partial \beta}\left(\frac{v}{R_2} + \frac{1}{B}\frac{\partial w}{\partial \beta}\right) - \frac{1}{AB}\frac{\partial B}{\partial \alpha}\left(\frac{u}{R_1} + \frac{1}{A}\frac{\partial w}{\partial \alpha}\right)$$
$$\text{and} \qquad \chi_{12} = -\frac{1}{AB}\left(\frac{\partial^2 w}{\partial \alpha\,\partial \beta} - \frac{1}{A}\frac{\partial A}{\partial \beta}\frac{\partial w}{\partial \alpha} - \frac{1}{B}\frac{\partial B}{\partial \alpha}\frac{\partial w}{\partial \beta}\right) - \frac{1}{R_1}\frac{A}{B}\frac{\partial}{\partial \beta}\left(\frac{u}{A}\right) - \frac{1}{R_2}\frac{B}{A}\frac{\partial}{\partial \alpha}\left(\frac{v}{B}\right).$$

Downloaded from https://royalsocietypublishing.org/ on 14 December 2022

In equations (2.12) and (2.14), the derivatives with respect to principal coordinates $\alpha\beta$ are not known beforehand for an arbitrary shape. However, the surface of the thin shell is simply defined by the global Cartesian coordinates xyz. Therefore, to transform the derivatives from $\alpha\beta$ coordinates to Cartesian coordinate xyz, the chain rule is applied, equation (2.9). Since the boundary conditions are in the form of displacements, equations (2.12)–(2.14) are simultaneously solved to give three partial differential equations in terms of unknown displacements u, v and w:

$$\begin{aligned}
&C_1\frac{\partial^3 w}{\partial x^3}+C_2\frac{\partial^3 w}{\partial x^2\partial y}+C_3\frac{\partial^3 w}{\partial x\partial y^2}+C_4\frac{\partial^3 w}{\partial y^3}+C_5\frac{\partial^2 u}{\partial x^2}+C_6\frac{\partial^2 u}{\partial x\partial y}+C_7\frac{\partial^2 u}{\partial y^2}\\
&\quad+C_8\frac{\partial^2 v}{\partial x^2}+C_9\frac{\partial^2 v}{\partial x\partial y}+C_{10}\frac{\partial^2 v}{\partial y^2}+C_{11}\frac{\partial^2 w}{\partial x^2}+C_{12}\frac{\partial^2 w}{\partial x\partial y}+C_{13}\frac{\partial^2 w}{\partial y^2}\\
&\quad+C_{14}\frac{\partial u}{\partial x}+C_{15}\frac{\partial u}{\partial y}+C_{16}\frac{\partial v}{\partial x}+C_{17}\frac{\partial v}{\partial y}+C_{18}\frac{\partial w}{\partial x}+C_{19}\frac{\partial w}{\partial y}+C_{20}u+C_{21}v+C_{22}w=0,\\
&C_{23}\frac{\partial^3 w}{\partial x^3}+C_{24}\frac{\partial^3 w}{\partial x^2\partial y}+C_{25}\frac{\partial^3 w}{\partial x\partial y^2}+C_{26}\frac{\partial^3 w}{\partial y^3}+C_{27}\frac{\partial^2 u}{\partial x^2}+C_{28}\frac{\partial^2 u}{\partial x\partial y}+C_{29}\frac{\partial^2 u}{\partial y^2}\\
&\quad+C_{30}\frac{\partial^2 v}{\partial x^2}+C_{31}\frac{\partial^2 v}{\partial x\partial y}+C_{32}\frac{\partial^2 v}{\partial y^2}+C_{33}\frac{\partial^2 w}{\partial x^2}+C_{34}\frac{\partial^2 w}{\partial x\partial y}+C_{35}\frac{\partial^2 w}{\partial y^2}\\
&\quad+C_{36}\frac{\partial u}{\partial x}+C_{37}\frac{\partial u}{\partial y}+C_{38}\frac{\partial v}{\partial x}+C_{39}\frac{\partial v}{\partial y}+C_{40}\frac{\partial w}{\partial x}+C_{41}\frac{\partial w}{\partial y}+C_{42}u+C_{43}v+C_{44}w=0\\
\text{and}\quad&C_{45}\frac{\partial^4 w}{\partial x^4}+C_{46}\frac{\partial^4 w}{\partial x^3\partial y}+C_{47}\frac{\partial^4 w}{\partial x^2\partial y^2}+C_{48}\frac{\partial^4 w}{\partial x\partial y^3}+C_{49}\frac{\partial^4 w}{\partial y^4}+C_{50}\frac{\partial^3 u}{\partial x^3}+C_{51}\frac{\partial^3 u}{\partial x^2\partial y}\\
&\quad+C_{52}\frac{\partial^3 u}{\partial x\partial y^2}+C_{53}\frac{\partial^3 u}{\partial y^3}+C_{54}\frac{\partial^3 v}{\partial x^3}+C_{55}\frac{\partial^3 v}{\partial x^2\partial y}+C_{56}\frac{\partial^3 v}{\partial x\partial y^2}+C_{57}\frac{\partial^3 v}{\partial y^3}+C_{58}\frac{\partial^3 w}{\partial x^3}\\
&\quad+C_{59}\frac{\partial^3 w}{\partial x^2\partial y}+C_{60}\frac{\partial^3 w}{\partial x\partial y^2}+C_{61}\frac{\partial^3 w}{\partial y^3}+C_{62}\frac{\partial^2 w}{\partial x^2}+C_{63}\frac{\partial^2 w}{\partial x\partial y}+C_{64}\frac{\partial^2 w}{\partial y^2}+C_{65}\frac{\partial^2 u}{\partial x^2}\\
&\quad+C_{66}\frac{\partial^2 u}{\partial x\partial y}+C_{67}\frac{\partial^2 u}{\partial y^2}+C_{68}\frac{\partial^2 v}{\partial x^2}+C_{69}\frac{\partial^2 v}{\partial x\partial y}+C_{70}\frac{\partial^2 v}{\partial y^2}+C_{71}\frac{\partial u}{\partial x}+C_{72}\frac{\partial u}{\partial y}\\
&\quad+C_{73}\frac{\partial v}{\partial x}+C_{74}\frac{\partial v}{\partial y}+C_{75}\frac{\partial w}{\partial x}+C_{76}\frac{\partial w}{\partial y}+C_{77}u+C_{78}v+C_{79}w+C_{80}=0.
\end{aligned}\tag{2.15}$$

The coefficients C_1–C_{80} in equation (2.15) are known functions of the deformed shape, shell thickness, material properties and applied pressure, i.e. $C_i = C_i\ (x, y, z, h, E, \nu, p)$. The first 10 coefficients, C_1–C_{10}, and C_{80} are given in appendix B as an example. It is worth noting that all the coefficients are independent of the elastic modulus E, except for C_{80}, in which E^{-1} is a common multiplicative factor that is separable. Therefore, the particular solution of the system of equation (2.15) is proportional to E^{-1}, further explained in appendix B. However, the resulting stresses become independent of Young's modulus after the displacement field is back substituted in equations (2.14) and (2.13), because of the presence of E in the constitutive equations. This result represents the cornerstone of the proposed forward elastostatic method to directly compute the stresses in thin shells of known arbitrarily deformed geometry, without requiring the full knowledge of the material response. In compressible materials, only Poisson's ratio, which remains an independent variable, should be assumed in the determination of the stresses. Whereas, in incompressible solids, the stress field can be directly computed without knowing any material parameters. Lastly, it should be noted that, differently from the stress state, the kinematic fields depend on the material parameters and they should be considered virtual

Downloaded from https://royalsocietypublishing.org/ on 14 December 2022

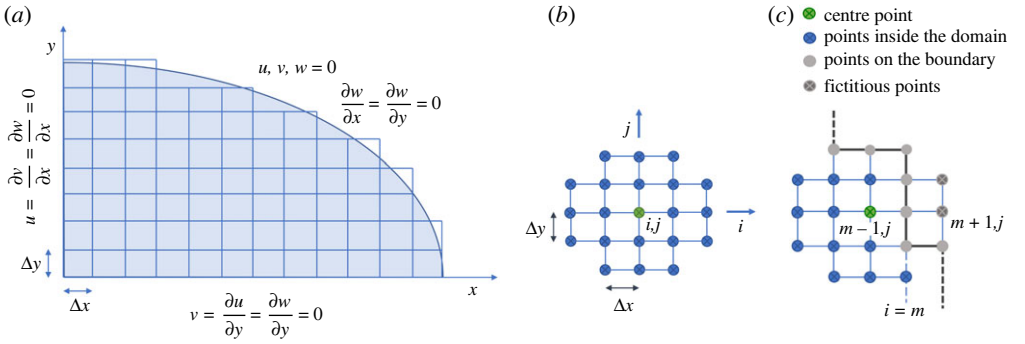

Figure 3. (*a*) Discretized quarter of elliptical domain along with the boundary conditions. (*b*) Stencil of points required for first to fourth order derivatives in the two-dimensional finite difference scheme. (*c*) Finite difference grid near the boundary region showing fictitious points outside the elliptical domain and points lying on the boundary. (Online version in colour.)

when the above formulation is employed in the direct stress determination for finite elasticity problems.

(c) Solution procedure through finite difference method

The system of equation (2.15) is applicable to any arbitrary shape of the shell surface that is given as $z = f(x, y)$ and can be solved for the unknown displacements u, v and w by a suitable method using prescribed boundary conditions. One of the common techniques used in solving boundary value problems is the FDM, where a spatial domain is discretized [49].

Various engineering problems can benefit from the presented formulation for the determination of the stress distribution in statically indeterminate shells of known spatial configurations when the material model is not available. One of which is the development of constitutive relations and parameters identification in soft materials through bulge testing at increasing pressures [50], where the deformed configurations can be measured through optical techniques, such as digital image correlation (DIC) [22,32]. In particular, the inflation of non-axisymmetric planar shells can be used to introduce unequal stresses at the apex of the deformed configuration. In this framework, a favourable choice is through elliptical samples having a continuous clamped edge, for which there are no available solutions to directly determine the stresses in the deformed shell.

Therefore, the formulation presented in the previous section is here applied to directly determine the stress state during finite elliptic bulge testing, and the FDM is implemented for elliptical shells. The finite difference formulae used to discretize equation (2.15) are presented in appendix C for the displacement w as a reference. The elliptical domain is discretized in x and y directions using uniform increments Δx and Δy. Exploiting symmetry, only one quarter of the ellipse is considered, shown in figure 3*a* along with the boundary conditions. Null displacements and rotations are prescribed on the curved boundary, while on the axes of symmetry, the perpendicular displacements are zero, along with the derivatives of the remaining displacement components. Since the curved boundary is approximated with a linear grid parallel to the x and y axes, the zero rotation condition can be written as

$$\frac{\partial w}{\partial x} = 0 \quad \text{and} \quad \frac{\partial w}{\partial y} = 0. \tag{2.16}$$

The highest derivative in equation (2.15) is of the fourth order, which implies that the approximation near the boundaries requires discretizing points outside the elliptical domain, as depicted by a stencil of points in figure 3*b*,*c*. For the normal displacement w, the boundary conditions at the curved edge ($w = 0$, $\partial w/\partial x = 0$ and $\partial w/\partial y = 0$) can be used to approximate the

Downloaded from https://royalsocietypublishing.org/ on 14 December 2022

higher-order derivatives. For example, the fourth order derivative of w with respect to x can be approximated as

$$\left.\frac{\partial^4 w}{\partial x^4}\right|_{i,j} = \frac{1}{\Delta x^4}\left(w_{i+2,j} - 4w_{i+1,j} + 6w_{i,j} - 4w_{i-1,j} + w_{i-2,j}\right), \tag{2.17}$$

where i and j represent the x and y position of the point, respectively. Denoting $w_{m,j}$ as the displacement of the point lying on the vertical segment of the curved boundary, figure 3*c*, the clamped conditions imply $w_{m,j} = 0$. Therefore, the discretized equations need to be written for i up to $m-1$, so that i can be replaced by $m-1$ in equation (2.17)

$$\left.\frac{\partial^4 w}{\partial x^4}\right|_{m-1,j} = \frac{1}{\Delta x^4}\left(w_{m+1,j} - 4w_{m,j} + 6w_{m-1,j} - 4w_{m-2,j} + w_{m-3,j}\right), \tag{2.18}$$

where $w_{m+1,j}$ is the fictitious point lying outside the considered domain. To find $w_{m+1,j}$, the central finite difference form of equation $(2.16)_1$ is written for the point (m, j) as

$$\left.\frac{\partial w}{\partial x}\right|_{m,j} = \frac{w_{m+1,j} - w_{m-1,j}}{2\Delta x} = 0 \Longrightarrow w_{m+1,j} = w_{m-1,j}, \tag{2.19}$$

implying that $w_{m+1,j}$ can be replaced by $w_{m-1,j}$ in the finite difference equations. Similarly, the displacement w of all fictitious points can be substituted with the displacement of the corresponding symmetric points lying inside the domain. For the displacement components u and v, the boundary conditions at the clamped edge do not include the derivatives of u and v. Hence, linear extrapolation is used to write the finite difference equations for the points lying outside the domain. It should be noted that the highest derivative for u and v in equation (2.15) is of the third order, thus requiring a fewer number of points than those illustrated in figure 3*b*.

The discretization of the system of differential equations (2.15) results in a system of linear equations, which is solved by the direct method to give u, v and w. The resulting displacement components are back substituted in equation (2.14) to find the strains, and subsequently, constitutive equations (2.13) are used to convert the strain components into stress resultants, from which the normal stresses for the middle surface, σ_1 and σ_2, can be calculated as

$$\sigma_1 = \frac{N_1}{h} \quad \text{and} \quad \sigma_2 = \frac{N_2}{h}. \tag{2.20}$$

As noted before, the displacement and strain components are functions of the material parameters, elastic modulus E and Poisson's ratio ν, but when they are back substituted in the constitutive relations, equation (2.13), the stresses become independent of E, and only ν affects the stress distribution for compressible materials. Hence, the small displacements and strains calculated through the finite difference code should be treated as virtual when nonlinear problems with deformable shells are considered, and only the stresses are useful. The stress distribution independence of E is of paramount importance, as it enables the direct stress determination in elastic shells of known arbitrary shape without requiring the knowledge of the full constitutive model.

Lastly, it is worth noting that the stresses can also be directly obtained through an equivalent finite-element forward elastostatic method, where linear analysis is performed on each deformed shell configuration. In this approach, validated in appendix D, the deformed shape is reconstructed in the finite-element software, and constitutes the reference configuration, in equilibrium with the external loads. Therefore, the equilibrated stress state from the linear analysis is independent of the subsequent deformations, which can be considered virtual, and of the material model employed, where linear elasticity can be assumed for simplicity.

Downloaded from https://royalsocietypublishing.org/ on 14 December 2022

3. Results and discussion

The presented forward elastostatic method is here applied to the determination of the stresses during inflation of elliptical shells and validated through finite-element analyses and experiments. The finite difference formulation was implemented in a Matlab script that can be found at https://github.com/fbosi/StressesEllipticBulging. The influence of Poisson's ratio on the stress distribution is presented in §3a, while in §3b, it is shown that the proposed method for direct stress measurements is applicable to nonlinear elastic materials.

(a) Comparison of the present solution with finite-element analysis

The first validation of the developed formulation and its finite difference implementation was performed through FEA run in Abaqus 2019 (Dassault Systèms). Elliptical planar shells of different aspect ratios, characterized by the major radius a, minor radius b and initial thickness h_0, were inflated by a normal uniform pressure p from the initial flat configuration, clamped at its edge. The initial thickness h_0 was 100 µm, a was fixed to 60 mm for all the analyses, whereas b was varied to achieve different aspect ratios. Geometric nonlinear FE analyses were performed using shell elements (S4 and S3), where a quarter of the elliptical shell was modelled, thanks to symmetry conditions. The elastic material model was characterized by Young's modulus $E = 2.5$ GPa and Poisson's ratio $\nu = 0.35$.

From the FEA results, each shell deformed shape was acquired in the form of (x, y, z) data points and thickness h for each node, and it was given as input to the finite difference code to calculate the stresses throughout the shell and compare them with the FEA stress field. A cubic interpolation ('griddata' in Matlab) was used to form the uniformly spaced finite difference grid (size between 0.25 and 1 mm) from the scattered nodal FEA data points. The base vectors $\mathbf{T}_\alpha$ and $\mathbf{T}_\beta$, and the surface parameters R_1, R_2, A and B, were obtained using the equations presented in §2a to initiate the finite difference code. Each deformed state of the inflated elliptical shell from FEA was processed independently to obtain the stress fields at each equilibrium configuration, thus making the finite difference code independent of the deformation history. A fictitious elastic modulus, $\bar{E} = 1$, was used in the finite difference scheme since the stresses are independent of Young's modulus, as observed in the previous section.

The normalized stresses along the major and minor axis of the inflated shell, $\sigma_1 b/Eh_0$ and $\sigma_2 b/Eh_0$, obtained from FEA and the finite difference formulation, are compared in figure 4 for an elliptical geometry with an aspect ratio of 0.5. The normalized stresses are plotted against the dimensionless major and minor radial coordinates x/a and y/b for deformation levels $z_0/b \approx [0.25, 0.5, 1]$, where z_0 represents the z coordinate at the apex of the deformed shell. The finite difference predictions (solid line) match well with the FEA results (dotted line) in all plots of figure 4 for $z_0/b \approx 0.25$ and $z_0/b \approx 0.5$, when the same value of Poisson's ratio, $\nu = 0.35$, is considered. However, for highly deformed configurations, $z_0/b \approx 1$, σ_1 shows some deviations in figure 4*a*,*c*. The difference between FEA and finite difference results is due to the pronounced change in curvature in the first direction R_1 (aligned with σ_1) for higher deformation levels, whereas, along y, the deformed shape resembles a cylinder with an almost uniform radius of curvature R_2. The higher gradients of R_1 are difficult to capture, especially near the ellipse's edge, where extrapolation is used and causes the discrepancies observed for σ_1. Nonetheless, the maximum error in σ_1, at the apex of the shell, remains under 5% for the highest deformation level $z_0/b \approx 1$. Above this deformation, the shell surface bulges out from its planar domain, which hinders the reconstruction of the deformed shape through a planar grid because the gradients of the surface become infinite. As noted before, the stress state in each deformed shape can also be obtained by means of independent finite-element forward elastostatic analyses performed on the reconstructed configurations. Each deformed equilibrium configuration obtained from the nonlinear FE finite inflation of planar elliptical shells with prescribed material properties was used as the reference state for a static linear analysis performed with the same software, owning a fictitious unit Young's modulus. The stress results obtained from the finite element forward

Downloaded from https://royalsocietypublishing.org/ on 14 December 2022

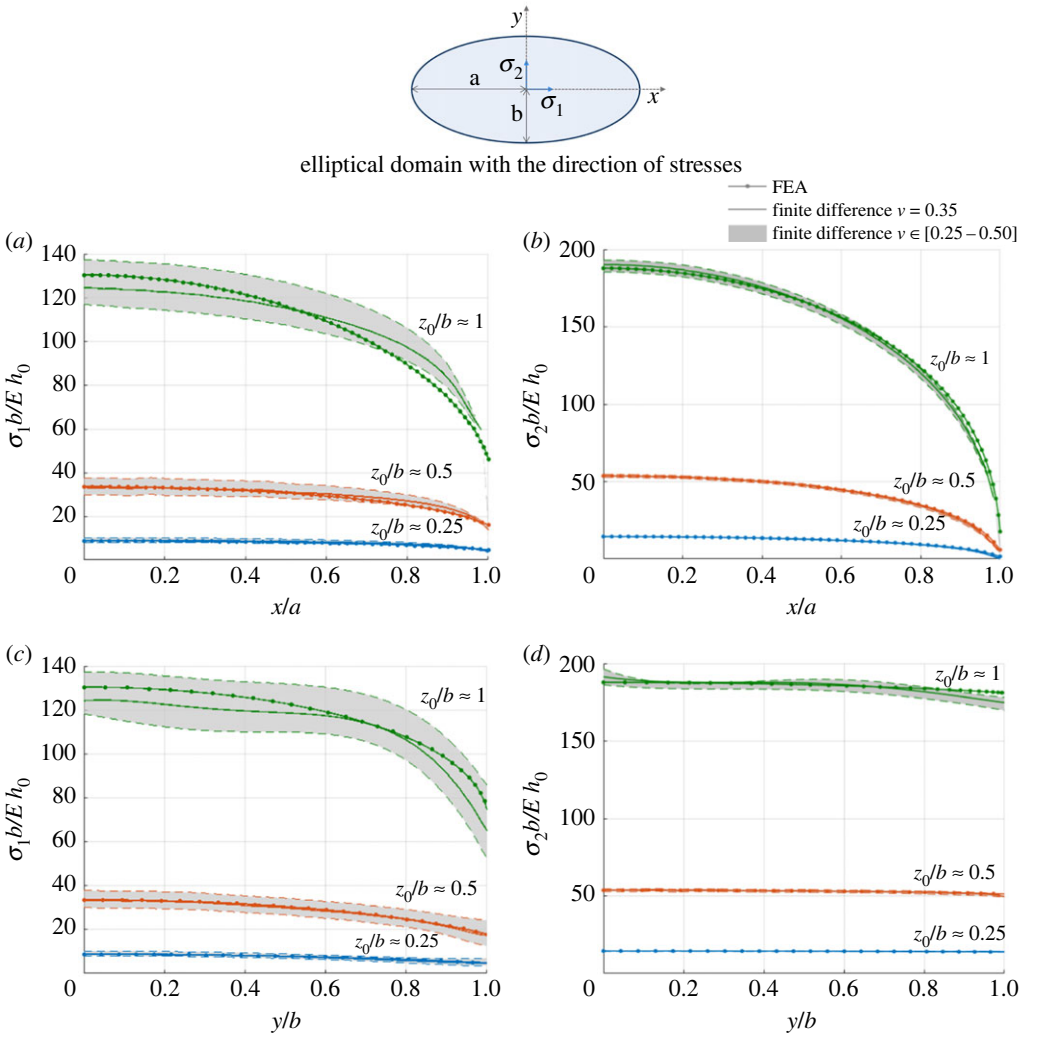

Figure 4. Normalized stress along the first principal direction, $\sigma_1 b/Eh_0$ (*a*,*c*), and second principal direction, $\sigma_2 b/Eh_0$ (*b*,*d*) plotted against the dimensionless coordinates x/a (*a*,*b*) and y/b (*c*,*d*) for $z_0/b \approx [0.25, 0.5, 1]$. The results from FE (solid line with dot) and finite difference forward elastostatic method (solid line) are compared for $\nu = 0.35$ during the inflation of planar elliptical shells with $b/a = 0.5$. The grey area within the dashed curves represents the present solution when $\nu \in [0.25 - 0.5]$. (Online version in colour.)

elastostatic analysis are reported in appendix D, figure 12, and compared with the predictions shown in figure 4, showing excellent agreement and testifying the validity of this alternative reconstructed FE approach.

The stress distribution obtained through the finite difference forward elastostatic method was shown to depend only on Poisson's ratio. Therefore, in order to assess its influence on the accuracy of the results, ν was varied from 0.25 to 0.5, which represents the classical range for most engineering materials. The different values of Poisson's ratio result in grey areas for each curve of figure 4, where the lower bound represents $\nu = 0.25$ and the upper bound is for $\nu = 0.5$. Overall, the range of Poisson's ratio produces a maximum of $\pm 10\%$ deviation from the mean stress value at the apex of the shell for σ_1 and $\pm 2\%$ deviation from the mean value of σ_2. The lower sensitivity of σ_2 to Poisson's ratio is due to the limited variation of curvature in the second principal direction, which makes the stresses more sensitive to the curvature rather than the Poisson's ratio. These results show that, for compressible materials, even in the absence of a known Poisson's ratio,

Downloaded from https://royalsocietypublishing.org/ on 14 December 2022

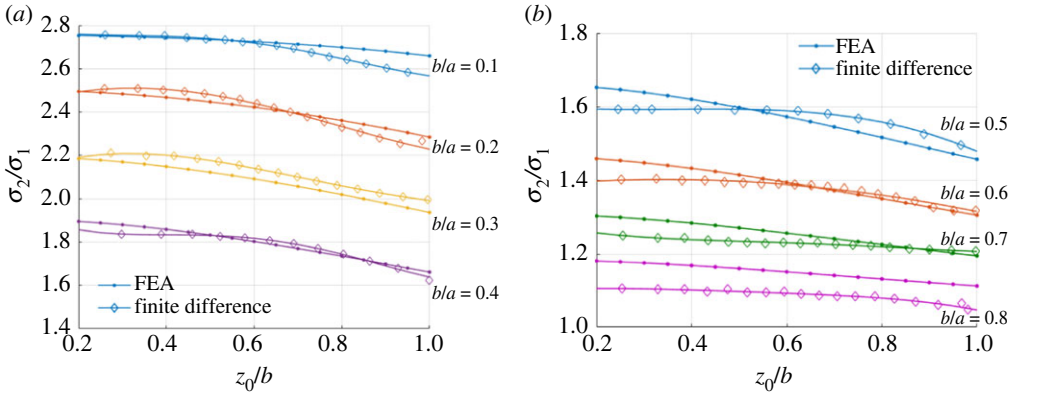

Figure 5. Stress ratio at the apex of the deformed thin shell, σ_2/σ_1, plotted against non-dimensional vertical position at the apex, z_0/b, for elliptical membrane with aspect ratios $b/a = [0.1, 0.2, 0.3, 0.4]$ (*a*) and $b/a = [0.5, 0.6, 0.7, 0.8]$ (*b*), obtained from FE (solid line with dot) and finite difference forward elastostatic (solid line with diamond) methods, with $\nu = 0.35$. (Online version in colour.)

and therefore without any knowledge of the material response, the proposed technique can still provide an accurate range of stresses throughout the entire shell by assuming an arbitrary, yet realistic, value for ν, with the accuracy that increases for less deformed (or shallow) shells.

To further compare the finite difference and the FE results for different aspect ratios throughout the entire deformation history, the stress ratio σ_2/σ_1 at the thin shell's apex is plotted against the dimensionless vertical position z_0/b in figure 5. The choice of plotting the stresses at the apex is motivated by the fact that those produce the highest equivalent stress and they are less disturbed by the edge effects during bulge tests. Both the finite difference and FE analyses were run for $b/a = [0.1, 0.2, 0.3, 0.4, 0.5, 0.6, 0.7, 0.8]$ and $\nu = 0.35$, with the results for aspect ratio higher than 0.5 shown in figure 5*b* for clarity. Overall there is a very good agreement between theoretical and FE results for all the aspect ratios and levels of deformation investigated. The maximum difference between the finite difference and FE results occurs for $b/a = 0.8$, although the error is amplified because the ratio between the stresses is shown. When the difference is calculated separately for the stress components, it is maximum 6% for σ_2 at $z_0/b \approx 0.25$ for $b/a = 0.8$. The source of discrepancy for a higher aspect ratio is due to the presence of a singularity of principal curvatures, which hinders the results in its proximity. At the singularity, the two principal curvatures become equal and the lines of principal curvature converge into one point. The point of singularity does not exist when $b/a < 0.5$, while it appears near the edge $x = a$ when $b/a = 0.5$, and moves towards the centre $x = 0$ when $b/a = 1$. For this reason, it is not advisable to use the current formulation for direct stress determination during the bulging of circular isotropic membranes. Instead, since that problem is statically determinate and equilibrium equations suffice, it is suggested to employ analytical solutions present in the literature for faster computation [32,33,51]. Alternatively, the present method can produce accurate results for the inflation of circular membranes by using the analytical expressions at the apex of the axisymmetric shape, where the singularity lies, and by applying the finite difference formulation to the remaining domain.

(b) Experimental validation through elliptical bulge tests

The developed forward elastostatic method and its finite difference implementation were employed in the direct determination of stresses during elliptic bulge experiments carried out on a hyperelastic material, in order to show the applicability of the proposed procedure also to nonlinear elastic solids. The finite difference code is devised using linear elastic constitutive equations, and in §2b it was shown that the calculation of stresses is independent of Young's modulus of the material. Since the formulation is based on small displacements on a known

Downloaded from https://royalsocietypublishing.org/ on 14 December 2022

equilibrium configuration of the shell, its applicability to nonlinear materials is justified because the nonlinear constitutive equations can be linearized for infinitesimal strains, as shown in appendix E for a hyperelastic constitutive relation. Hence, the script based on linear elasticity can be used to compute the stresses in non-axisymmetric shells made of a nonlinear elastic material.

(i) Material characterization

Thermoplastic polyurethane (TPU) membrane of thickness $h_0 = 110 \pm 10\,\mu$m (Elastollan C 85-A from BASF) was chosen because of its highly deformable elastomeric characteristics. First, uniaxial tensile and axisymmetric biaxial inflation tests were performed at room temperature to determine the stress–strain response of TPU and to model its constitutive behaviour necessary for the FE predictions of the inflation of elliptical thin shells. The uniaxial specimens were cut into the dumbbell shape according to ASTM D412-16 (Type A). An Instron 5985 electromechanical testing machine, fitted with 2 kN 2713-004 self-tightening grips and a 500 N load cell, was used to test the material [52]. Second, for the axisymmetric biaxial inflation test, a custom-made pressure chamber with a circular cut of 100 mm diameter was used to clamp the membrane at its periphery through fasteners [21]. Additionally, the chamber has an inlet port for air pressure and LED lights inside to illuminate the background of the transparent sample for DIC measurements. The high-pressure air is supplied to the testing system and is controlled by an onboard electric valve (Omega IP610-030) that regulates output air pressure in the range 0–30 psi. The pressure control valve uses 4–20 mA of current generated by onboard circuitry that includes a DC power supply and a current transmitter AD694. The transmitter converts 0–10 V DC analogue voltage from the computer, provided through a NI data acquisition system (DAQ) and a LabVIEW Signal Express script, to 4–20 mA of current. An electrical pressure gauge (Omega DPG409-015G) is used to display and send the pressure data of the chamber to the computer through the same DAQ in the form of 0 to 10 V analogue voltage.

The surface strains for both uniaxial and biaxial tests were measured through the DIC technique, where two stereo 5 MP cameras (Basler), equipped with Schneider Kreuznach Xenoplan lenses (focal length 35 mm), were held at an angle of $\sim 30^\circ$. The images were captured from the cameras using Vic-Snap software and were post-processed on Vic-3D (Correlated Solutions). Uniaxial experiments were performed in two orthogonal directions of the material to inspect the anisotropy, and the material was found to be isotropic. Therefore, for the biaxial inflation test, equilibrium equations under the material isotropy assumption were used to obtain the equibiaxial true stresses at the apex of the membrane, $\sigma = pr/(2h)$, where r represents the radius of curvature [32,33]. Poisson's ratio was measured with DIC during uniaxial tensile tests from the transverse and longitudinal strains, and it was found to be ≈ 0.5. Hence, the mean true stress–strain response for TPU films was calculated using the incompressibility assumption from three uniaxial tensile tests and three biaxial inflation tests, shown in figure 6*a*,*b*, respectively. The strain rate for these tests was kept in the range 0.1–0.2%/s, which corresponds to the strain rate at the apex of the membrane during the next set of inflation tests on elliptical membranes.

The stress–strain data from figure 6 were used to calibrate the hyperelastic material model required as input in Abaqus 2019 to obtain the FE predictions of stresses in any deformed configuration during inflation [53]. These FE results will serve as a reference for comparison with the experimentally derived stresses obtained from the presented forward elastostatic formulation, which do not require the knowledge of the constitutive model. The material hyperelastic response was modelled through a fifth-degree polynomial strain energy function, whose coefficients are reported in appendix E, Table 1, and were used in the Abaqus subroutine UHYPER to predict the stresses in the TPU membrane during FE elliptical inflation, as described in the next section. For the fitting, the strain energy density corresponding to different values of the Cauchy–Green strain invariants I_1 and I_2 was calculated from the uniaxial and biaxial test data. The comparison between the fitted model and the experimental data for uniaxial and biaxial response is shown in figure 7*a*,*b*, respectively.

Downloaded from https://royalsocietypublishing.org/ on 14 December 2022

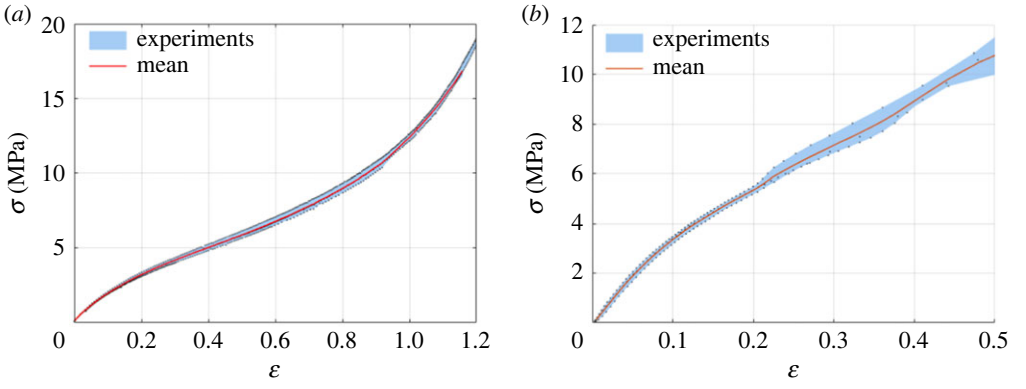

Figure 6. True stress–strain response of TPU membranes from uniaxial tensile tests (*a*) and biaxial inflation experiments (*b*), showing average (red curve) and raw (blue region and dots) data. (Online version in colour.)

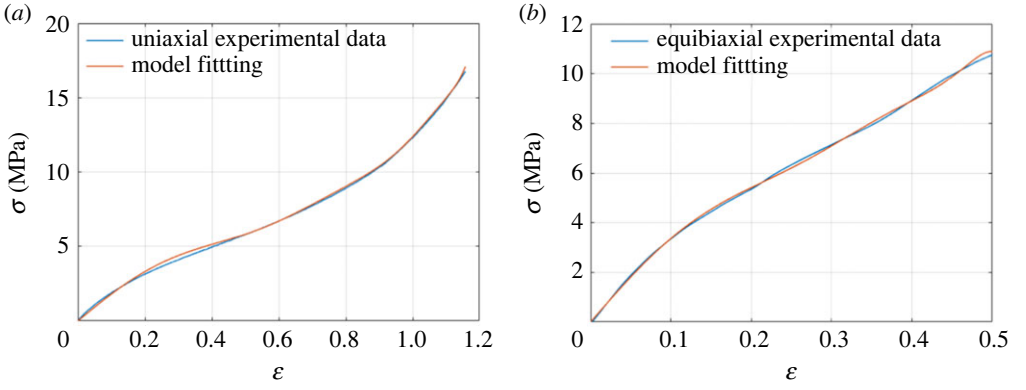

Figure 7. Comparison between uniaxial (*a*) and equibiaxial (*b*) experimental data and the hyperelastic model predictions obtained through a fifth-degree polynomial fitting of the strain energy density function. (Online version in colour.)

(ii) Stress determination during elliptical bulge experiments

The elliptical diaphragm inflation tests were performed in a pressure chamber similar to the one employed for the circular inflation set-up. The chamber has multiple configurations for elliptical inner cuts with major radius $a = 60$ mm and minor radii b of 30 mm and 42 mm to provide 0.5 and 0.7 aspect ratios, respectively. The rest of the components for the elliptical inflation test remain the same as in the circular inflation experiments described in the previous section.

The deformed shape, principal curvatures and directions were extracted from DIC, while the thickness of the shell was computed using the incompressibility assumption from the surface strains. The data were processed using the Matlab finite difference code to calculate the stresses in the principal directions of the inflated membrane for each deformed state. A uniform grid of 0.5 mm was used to export the data from DIC. However, due to the finite box size used for DIC correlation, the data near the edge of the sample could not be computed. Therefore, a linear surface extrapolation function in Matlab ('scatteredInterpolant') was used to fill the gaps near the boundary and perform the calculations. In addition to the extrapolation, a smoothing spline function in Matlab ('spaps') was employed to reduce the noise of the DIC data. The code also requires the pressure values, which were measured by the DIC software through the DAQ, at each deformed shape.

Three inflation tests were performed on TPU films using the elliptical pressure chamber of 0.5 aspect ratio, and the results are presented in figure 8, along with the predictions from the nonlinear FEA simulation. The principal stresses at the apex of the membrane are plotted against

Downloaded from https://royalsocietypublishing.org/ on 14 December 2022

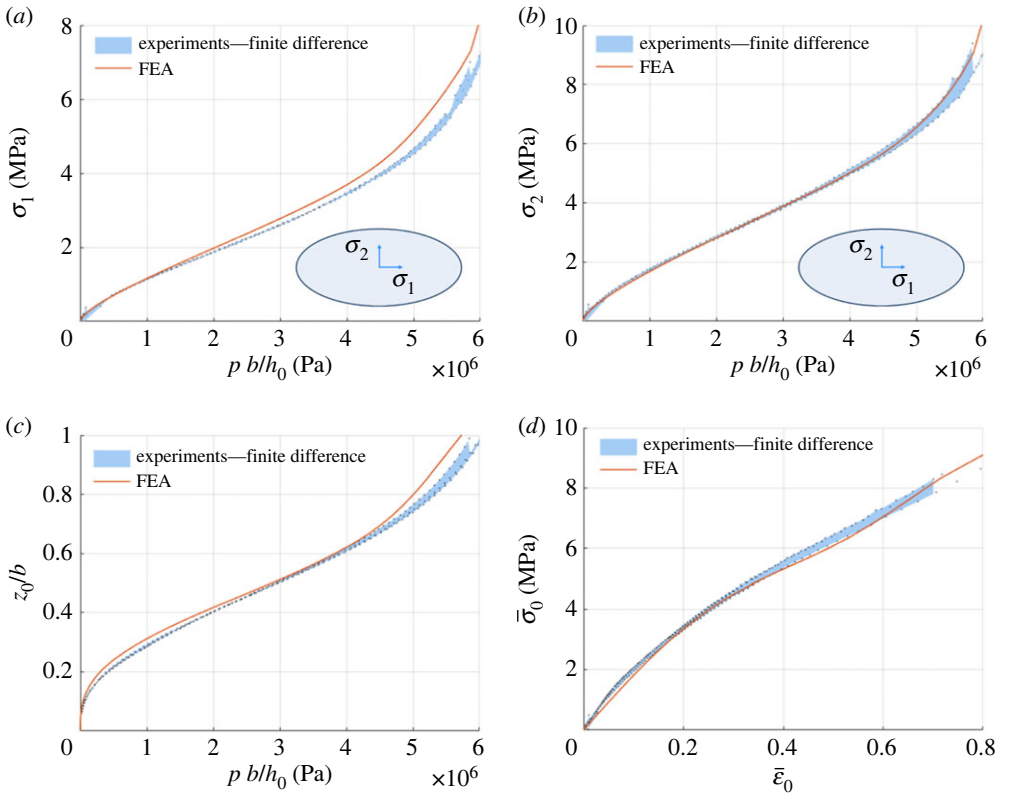

Figure 8. Comparison between FEA (red curve) and finite difference experimental (blue region and dots) results for the diaphragm inflation of elliptical TPU membranes of aspect ratio $b/a = 0.5$. The stresses in the first σ_1 (*a*) and second σ_2 (*b*) principal directions, and the dimensionless vertical position z_0/b (*c*) at the apex of the membrane are plotted against normalized pressure $p\,b/h_0$. (*d*) Equivalent stress $\bar{\sigma}_0$ versus equivalent strain $\bar{\varepsilon}_0$ at the apex of the membrane. (Online version in colour.)

the normalized pressure pb/h_0 in figure 8*a*,*b*, while the vertical position of the apex, normalized by the minor radius of the membrane, z_0/b, is plotted against the normalized pressure in figure 8*c* for both the experimental and FEA results. In the horizontal axis of figure 8, the pressure is multiplied by the factor b/h_0 to normalize the effects of initial thickness, which is ±10% for the tested TPU samples. The results show a very good agreement, as the FE curves lie very close to the experimental data, obtained through the finite difference code. The minor discrepancies are due to the fitting deviations evident in figure 7*a*,*b*. The vertical displacement plot of figure 8*c* is a direct result of the DIC measurements, which do not involve the finite difference code and show the high fidelity of the calibrated hyperelastic model. The plot of equivalent stress $\bar{\sigma}_0$ versus equivalent strain $\bar{\epsilon}_0$ at the apex of the membrane is shown in figure 8*d*, which also depicts good agreement between nonlinear FE predictions and finite difference elastostatic calculations. Alternatively to the finite difference analysis, forward linear elastic finite-element simulations can be performed starting from the deformed experimental configuration used as the reference state, with any fictitious incompressible material model. The forward finite-element predictions of the stresses σ_1 and σ_2 obtained from the reconstructed measured geometries are added to the plots of figure 8*a*,*b* and shown in appendix D, figure 13.

Experiments were also performed on the 0.7 aspect ratio elliptical membrane, and the deformed shapes were post-processed to directly calculate the stresses using the developed formulation and the finite difference code. Nonlinear FE simulations were carried out for the 0.7 aspect ratio ellipse, and the results are added for comparison in figure 9. The principal

Downloaded from https://royalsocietypublishing.org/ on 14 December 2022

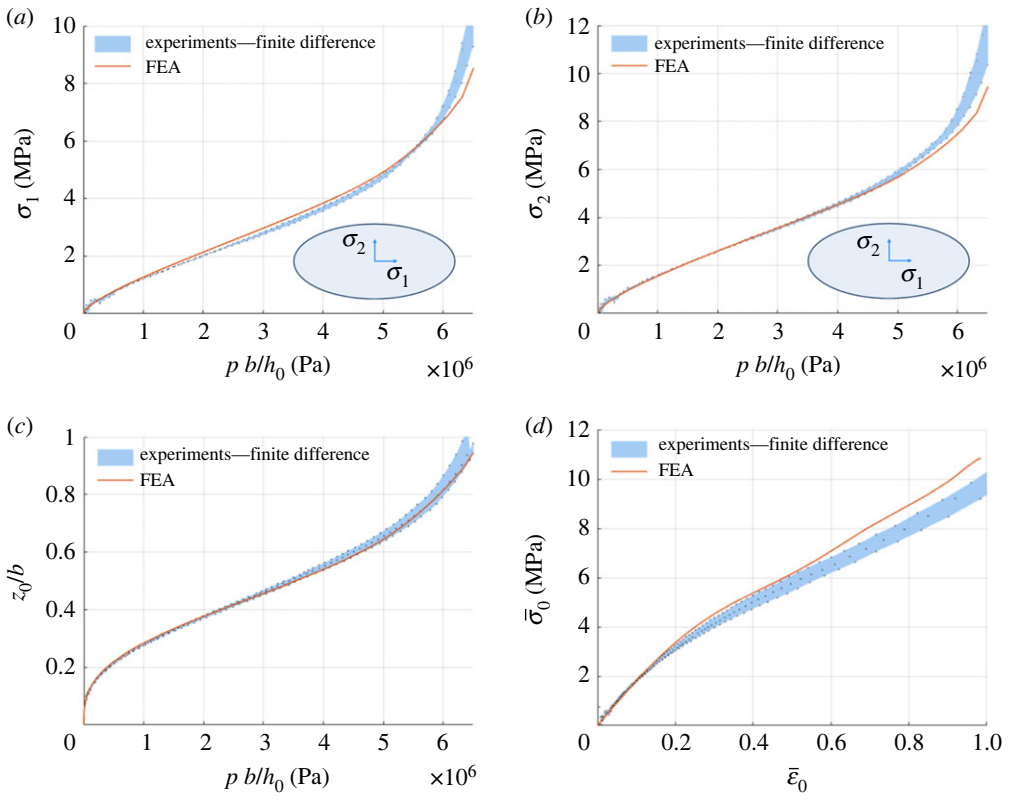

Figure 9. Comparison between FEA (red curve) and finite difference experimental (blue region and dots) results for the diaphragm inflation of elliptical TPU membranes of aspect ratio $b/a = 0.7$. The stresses in the first σ_1 (*a*) and second σ_2 (*b*) principal directions, and the dimensionless vertical position z_0/b (*c*) at the apex of the membrane are plotted against normalized pressure $p\,b/h_0$. (*d*) Equivalent stress $\bar{\sigma}_0$ versus equivalent strain $\bar{\varepsilon}_0$ at the apex of the membrane. (Online version in colour.)

stresses at the apex of the membrane, figure 9*a*,*b*, and the vertical position, figure 9*c*, show very good agreement for all the normalized pressure values. Similarly, the equivalent stress versus equivalent strain plot from experiments and FEA shows a good match, figure 9*d*. Overall, the results from the inflation of two different aspect ratios of TPU elliptical membranes (figures 8 and 9) prove a very good accuracy of the stress computation through the newly developed finite difference forward elastostatic formulation, where the deformation levels reach up to the minor radius, $z_0/b \approx 1$.

In addition to the results extracted at the apex of the membrane, the full-field plots of first, σ_I, and second, σ_{II}, principal stresses, directly obtained during TPU inflation, are compared with the FEA contour plots in figure 10 for the deformation levels of $z_0/b \approx 0.25$ and $z_0/b \approx 0.5$. The stress contours from FEA and experiments of figure 10*a*,*b* match to a great extent, while the difference near the curved edge is due to the intrinsic noise in the DIC measurement of the radii of principal curvatures and the smoothing function, which affects the accuracy of extracted results, especially in the areas of sharp gradients. The noise of DIC is higher at small deformation, while it decreases as the shell is inflated more. The effect of decreasing noise results in improved accuracy for figure 10*c*,*d*, when $z_0/b \approx 0.5$. In particular, throughout the entire shell, the mean absolute percentage difference between the experimental and FE predictions for $z_0/b \approx 0.25$ is 6.74% and 7.61% for σ_I and σ_{II}, respectively, while for $z_0/b \approx 0.5$ is 2.45% and 7.17% for σ_I and σ_{II}, respectively. The grey area around the curved edge for the experimental contour plots of figure 10 shows the lack of DIC data due to the finite size of the box chosen for image correlation and the edge shadow. In all plots of figure 10, the location of the maximum principal

Downloaded from https://royalsocietypublishing.org/ on 14 December 2022

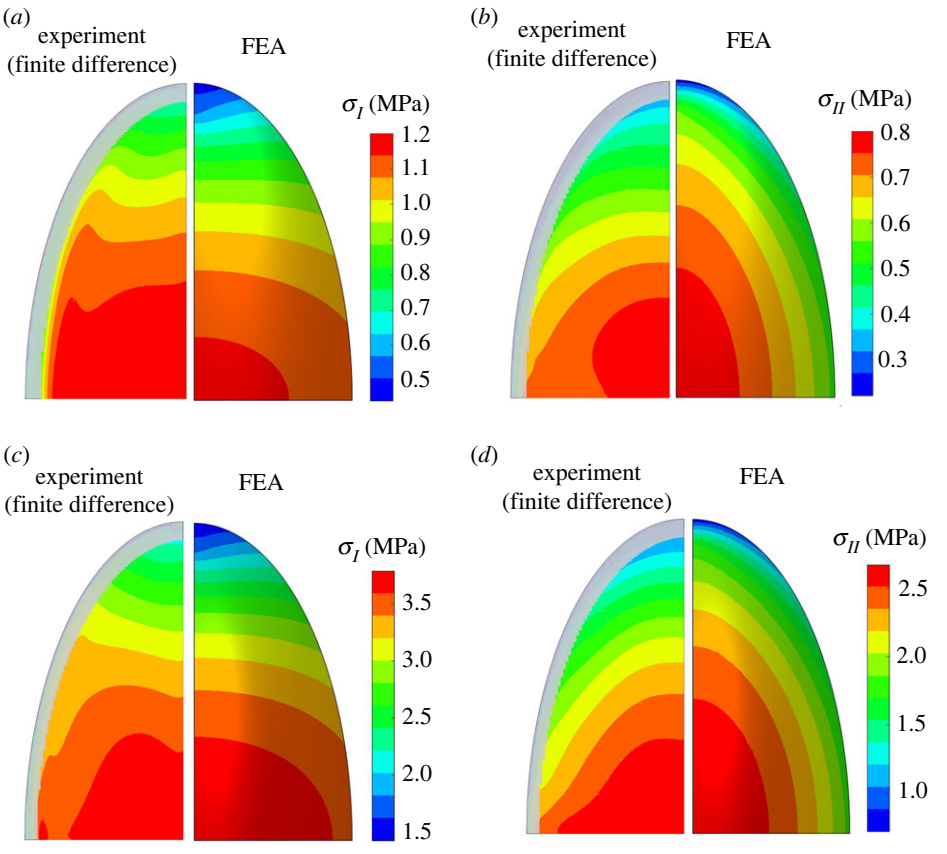

Figure 10. Comparison of principal stresses between FEA and finite difference experimental results for the diaphragm inflation of elliptical TPU membranes of aspect ratio $b/a = 0.5$. σ_I (*a*,*c*) and σ_{II} (*b*,*d*) are shown for $z_0/b \approx 0.25$ (*a*,*b*) and $z_0/b \approx 0.5$ (*c*,*d*). (Online version in colour.)

stresses appears at the apex, where the FEA and experiments show the best agreement between each other.

An important aspect of the finite difference formulation is represented by its ability to determine the stresses in elastic shells without the knowledge of material parameters. Indeed, in the developed formulation, the experimental stresses can be directly calculated from imaging measurements without using any information on the constituent material property, except for its Poisson's ratio for compressible solids. Furthermore, it can be used with highly nonlinear elastic materials. Although TPU has a varying tangent modulus E_t, as can be seen in figure 7*a*,*b*, a fictitious value of constant elastic modulus $\bar{E} = 1$ was used in the finite difference code to determine the stresses throughout the entire samples. These outcomes show that the proposed forward elastostatic method and its numerical implementation yield promising results for the direct calculation of the stress distribution in elastic and homogeneous statically indeterminate shells, with applications ranging from the assessment of biological membranes to the determination of constitutive models, especially for anisotropic materials.

4. Conclusion

A forward elastostatic method for the direct stress determination in thin shells of arbitrary shapes has been introduced and implemented through a finite difference procedure. The presented linear thin shell formulation is general and applicable to any small displacement problems of statically indeterminate shells under uniform pressure to give the complete deformation response when

Downloaded from https://royalsocietypublishing.org/ on 14 December 2022

the constitutive relation of the material is known. However, the major strength of the proposed work lies in the ability to directly measure the stresses, under virtual kinematic fields, during finite deformation of elastic shells in the absence of material properties, starting from the known deformed shapes, boundary and loading conditions. The only material property required by the developed formulation, solely for compressible solids, is Poisson's ratio, which is shown to have a limited influence on the stress distribution and therefore can be assumed without loss of accuracy.

The proposed method has been validated and used to determine the stresses in non-axisymmetric inflatable planar elliptical membranes without knowing the constituent material properties. Firstly, the developed procedure is applied to a compressible elastic material and the deformed shapes obtained from finite-element analysis of shell inflation. A good agreement is found for the stresses along the major and minor axes of an elliptical shell with a 0.5 aspect ratio, as well as the stresses at the apex for aspect ratios that range between 0.1 and 0.8, until the height of the deformed shape approaches the ellipse's minor radius. Secondly, the finite difference code is applied to directly compute the stresses from imaging measurements during the experimental inflation of nonlinear incompressible TPU elliptic diaphragms of $110 \pm 10\,\mu$m thickness, for 0.5 and 0.7 aspect ratios. The finite difference results, obtained without using any information on the material response, have been found in good agreement with the stresses computed through nonlinear finite-element analysis by using a calibrated hyperelastic model for TPU. Lastly, for both sets of validations, a finite-element forward elastostatic analysis on reconstructed deformed configurations has been proven as a valid alternative to the finite difference approach.

These outcomes show that the proposed technique and its numerical implementation yield promising results for the direct calculation of the stress distribution in elastic and homogeneous shells, with applications ranging from the determination of constitutive models through bulge tests to the assessment of non-axisymmetric thin shell structures. In particular, the presented method is expected to be advantageous in inverse problems, where the stress state in non-axisymmetric bulge tests can be measured independently from the strain field through imaging techniques, and it can be employed for the development of constitutive models and parameters identification when the material response is unknown. The application of the method in developing material models for structural membranes and its extension to non-axisymmetric elastoplastic bulging represent future avenues of research.

Data accessibility. The developed finite difference code and some examples can be found at https://github.com/fbosi/StressesEllipticBulging. Additional data are available on request from the corresponding author.

Authors' contributions. K.S.: data curation, formal analysis, investigation, methodology, software, validation, visualization, writing—original draft, writing—review and editing; F.B.: conceptualization, funding acquisition, investigation, methodology, project administration, supervision, validation, writing—review and editing.

Both authors gave final approval for publication and agreed to be held accountable for the work performed therein.

Conflict of interest declaration. We declare we have no competing interests.

Funding. The authors acknowledge support from the EU H2020-MSCA-ITN-2020-LIGHTEN-956547.

Appendix A. Definition of stress resultants and moments in thin shells

An infinitesimal element of a thin shell is reported in figure 11, where α and β represent the principal curvature coordinates, while ξ is the normal coordinate that ranges from $-h/2$ to $h/2$. The stress resultants and moments acting on each face of the thin shell can be obtained by integrating over the thickness direction the stress components highlighted in the figure [45]

$$N_1 = \int_{-h/2}^{h/2} \sigma_1^{\xi} \left(1 - \frac{\xi}{R_2}\right) \mathrm{d}\xi, N_2 = \int_{-h/2}^{h/2} \sigma_2^{\xi} \left(1 - \frac{\xi}{R_1}\right) \mathrm{d}\xi,$$

$$N_{12} = \int_{-h/2}^{h/2} \tau_{12}^{\xi} \left(1 - \frac{\xi}{R_2}\right) \mathrm{d}\xi$$

Downloaded from https://royalsocietypublishing.org/ on 14 December 2022

$$N_{21} = \int_{-h/2}^{h/2} \tau_{21}^{\xi} \left(1 - \frac{\xi}{R_1}\right) \mathrm{d}\xi, M_1 = \int_{-h/2}^{h/2} \sigma_1^{\xi}\, \xi \left(1 - \frac{\xi}{R_2}\right) \mathrm{d}\xi, \tag{A 1}$$

$$M_2 = \int_{-h/2}^{h/2} \sigma_2^{\xi}\, \xi \left(1 - \frac{\xi}{R_1}\right) \mathrm{d}\xi$$

and

$$H = \int_{-h/2}^{h/2} \tau_{12}^{\xi}\, \xi \left(1 - \frac{\xi}{R_1}\right) \mathrm{d}\xi = \int_{-h/2}^{h/2} \tau_{21}^{\xi}\, \xi \left(1 - \frac{\xi}{R_2}\right) \mathrm{d}\xi.$$

Furthermore, the stress components can be written in terms of stress resultants and moments at any normal coordinate ξ as [45]

$$\sigma_1^{\xi} = \frac{N_1}{h} + \frac{12M_1}{h^3}\xi$$

$$\sigma_2^{\xi} = \frac{N_2}{h} + \frac{12M_2}{h^3}\xi \tag{A 2}$$

and

$$\tau_{12}^{\xi} = \frac{1}{2h}(N_{12} + N_{21}) + \frac{6}{h^3}(M_{12} + M_{21})\xi.$$

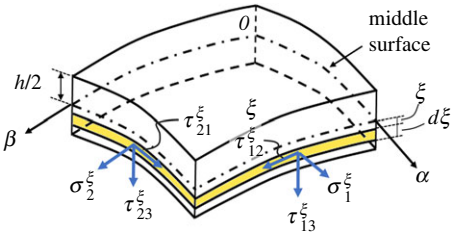

Figure 11. Three-dimensional view of an infinitesimal thin shell element of thickness h showing the stress components in the $\alpha\beta$ and normal coordinate system. (Online version in colour.)

Appendix B. Coefficients of the PDEs and solution procedure

The first 10 coefficients, C_1–C_{10}, and C_{80} from equation (2.15) are given below as an example. Similar expressions exist for the coefficients C_{11}–C_{79}, which are not reported here due to their lengthy forms. They can be found in the script developed for the finite difference solution of equation (2.15), available at https://github.com/fbosi/StressesEllipticBulging.

$$C_1 = \frac{1}{12A^2BR_1}\frac{\partial x}{\partial \alpha} h^2 \left(B^2 \frac{\partial x}{\partial \alpha}^2 - A^2 \frac{\partial x}{\partial \beta}^2 (\nu - 2)\right)$$

$$C_2 = \frac{1}{12A^2BR_1} h^2 \left(3B^2 \frac{\partial x}{\partial \alpha}^2 \frac{\partial y}{\partial \alpha} - A^2 \frac{\partial x}{\partial \beta} \left(2\frac{\partial x}{\partial \alpha}\frac{\partial y}{\partial \beta} + \frac{\partial x}{\partial \beta}\frac{\partial y}{\partial \alpha}\right)(\nu - 2)\right)$$

$$C_3 = \frac{1}{12A^2BR_1} h^2 \left(3B^2 \frac{\partial x}{\partial \alpha}\frac{\partial y}{\partial \alpha}^2 - A^2 \frac{\partial y}{\partial \beta} \left(\frac{\partial x}{\partial \alpha}\frac{\partial y}{\partial \beta} + 2\frac{\partial x}{\partial \beta}\frac{\partial y}{\partial \alpha}\right)(\nu - 2)\right)$$

$$C_4 = \frac{1}{12A^2BR_1}\frac{\partial y}{\partial \alpha} h^2 \left(B^2 \frac{\partial y}{\partial \alpha}^2 - A^2 \frac{\partial y}{\partial \beta}^2 (\nu - 2)\right)$$

$$C_5 = \frac{1}{12ABR_1^2} \left(B^2 \frac{\partial x}{\partial \alpha}^2 (12R_1^2 + h^2) - 2A^2 \frac{\partial x}{\partial \beta}^2 (3R_1^2 + h^2)(\nu - 1)\right) \tag{B 1}$$

$$C_6 = \frac{1}{6ABR_1^2} \left(B^2 \frac{\partial x}{\partial \alpha}\frac{\partial y}{\partial \alpha}(12R_1^2 + h^2) - 2A^2 \frac{\partial x}{\partial \beta}\frac{\partial y}{\partial \beta}(3R_1^2 + h^2)(\nu - 1)\right)$$

Downloaded from https://royalsocietypublishing.org/ on 14 December 2022

$$C_7 = \frac{1}{12\,A\,B\,{R_1}^2}\left(B^2\,\frac{\partial y}{\partial \alpha}^2\,(12\,{R_1}^2 + h^2) - 2\,A^2\,\frac{\partial y}{\partial \beta}^2\,(3\,{R_1}^2 + h^2)\,(\nu - 1)\right)$$

$$C_8 = -\frac{1}{12\,R_1\,R_2}\,\frac{\partial x}{\partial \alpha}\,\frac{\partial x}{\partial \beta}\,(h^2\,(\nu - 2) - 6\,R_1\,R_2\,(\nu + 1))$$

$$C_9 = -\frac{1}{12\,R_1\,R_2}(h^2\,(\nu - 2) - 6\,R_1\,R_2\,(\nu + 1))\left(\frac{\partial x}{\partial \alpha}\,\frac{\partial y}{\partial \beta} + \frac{\partial x}{\partial \beta}\,\frac{\partial y}{\partial \alpha}\right)$$

$$C_{10} = -\frac{1}{12\,R_1\,R_2}\,\frac{\partial y}{\partial \alpha}\,\frac{\partial y}{\partial \beta}\,(h^2\,(\nu - 2) - 6\,R_1\,R_2\,(\nu + 1))$$

and

$$C_{80} = \frac{1}{E}\,\frac{(1 - \nu^2)\,p\,A\,B}{h}.$$

The expressions for C_1–C_{80} and the finite difference formulae from equation (C 1) can be substituted into equation (2.15) to obtain three algebraic equations written for each point of the finite difference grid that discretize the domain, figure 3*a*. Denoting $\bar{n}$ as the total number of points in the grid, the resulting system has a total of $3 \times \bar{n}$ algebraic equations that can be represented in a matrix equation as

$$\mathbf{D}\mathbf{X} = \mathbf{Q}, \tag{B 2}$$

where $\mathbf{D}$ is a square coefficient matrix whose elements are the functions of C_1–C_{79}, $\mathbf{X}$ is the unknown column vector representing the displacement components u, v and w for all grid points and the vector $\mathbf{Q}$ is formed by the constant terms of the system of equations, all null except for those associated with the third equation of the system (2.15), which are equal to $-C_{80}$ for all points. Since the multiplicative factor E^{-1} appearing in the expression of C_{80} can be separated on the right-hand side of equation (B 2), the unknown vector $\mathbf{X}$ can be found as

$$\mathbf{X} = E^{-1}\mathbf{D}^{-1}\mathbf{Q}', \tag{B 3}$$

where $\mathbf{Q} = E^{-1}\mathbf{Q}'$. This implies that the particular solution of equation (2.15) and the resulting strains, equation (2.14), have a common multiplicative factor E^{-1}, which will be cancelled when the stresses are calculated through the constitutive relation equation (2.13), thus proving the independency of the stress state on the elastic modulus.

Appendix C. Finite difference formulae

The finite difference formulae for the displacement component w obtained by Taylor series expansion and using the method of undetermined coefficients are given below. Similar equations, employed in §2c, can be written for the other displacement components by substituting w with u or v.

$$\frac{\partial w}{\partial x} = \frac{w_{i+1,j} - w_{i-1,j}}{2\Delta x}$$

$$\frac{\partial w}{\partial y} = \frac{w_{i,j+1} - w_{i,j-1}}{2\Delta y}$$

$$\frac{\partial^2 w}{\partial x^2} = \frac{w_{i-1,j} - 2w_{i,j} + w_{i+1,j}}{\Delta x^2}$$

$$\frac{\partial^2 w}{\partial x \partial y} = \frac{w_{i-1,j-1} - w_{i-1,j+1} - w_{i+1,j-1} + w_{i+1,j+1}}{4\Delta x \Delta y}$$

$$\frac{\partial^2 w}{\partial y^2} = \frac{w_{i,j-1} - 2w_{i,j} + w_{i,j+1}}{\Delta y^2}$$

$$\frac{\partial^3 w}{\partial x^3} = \frac{1}{2\Delta x^3}\left(w_{i+2,j} - 2w_{i+1,j} + 2w_{i-1,j} - w_{i-2,j}\right)$$

Downloaded from https://royalsocietypublishing.org/ on 14 December 2022

$$\frac{\partial^3 w}{\partial x \partial y^2} = \frac{1}{2\Delta x \Delta y^2}\left(w_{i+1,j+1} + w_{i+1,j-1} - w_{i-1,j+1} - w_{i-1,j-1} + 2w_{i-1,j} - 2w_{i+1,j}\right)$$

$$\frac{\partial^3 w}{\partial x^2 \partial y} = \frac{1}{2\Delta x^2 \Delta y}\left(w_{i+1,j+1} - w_{i+1,j-1} + w_{i-1,j+1} - w_{i-1,j-1} - 2w_{i,j+1} + 2w_{i,j-1}\right)$$

$$\frac{\partial^3 w}{\partial y^3} = \frac{1}{2\Delta y^3}\left(w_{i,j+2} - 2w_{i,j+1} + 2w_{i,j-1} - w_{i,j-2}\right)$$

$$\frac{\partial^4 w}{\partial x^4} = \frac{1}{\Delta x^4}\left(w_{i+2,j} - 4w_{i+1,j} + 6w_{i,j} - 4w_{i-1,j} + w_{i-2,j}\right)$$

$$\frac{\partial^4 w}{\partial x^3 \partial y} = \frac{1}{4\Delta x^3 \Delta y}\left(w_{i+2,j+1} - 2w_{i+1,j+1} + 2w_{i-1,j+1} - w_{i-2,j+1} - w_{i+2,j-1} + 2w_{i+1,j-1} - 2w_{i-1,j-1} - w_{i-2,j-1}\right)$$

$$\frac{\partial^4 w}{\partial x^2 \partial y^2} = \frac{1}{\Delta x^2 \Delta y^2}\left(w_{i+1,j+1} - 2w_{i+1,j} + w_{i+1,j-1} - 2w_{i,j+1} + 4w_{i,j} - 2w_{i,j-1} + w_{i-1,j+1} - 2w_{i-1,j} + w_{i-1,j-1}\right)$$

$$\frac{\partial^4 w}{\partial x \partial y^3} = \frac{1}{4\Delta x \Delta y^3}\left(w_{i+1,j+2} - 2w_{i+1,j+1} + 2w_{i+1,j-1} - w_{i+1,j-2} - w_{i-1,j+2} + 2w_{i-1,j+1} - 2w_{i-1,j-1} - w_{i-1,j-2}\right)$$

and

$$\frac{\partial^4 w}{\partial y^4} = \frac{1}{\Delta y^4}\left(w_{i,j+2} - 4w_{i,j+1} + 6w_{i,j} - 4w_{i,j-1} + w_{i,j-2}\right). \tag{C 1}$$

Appendix D. Finite-element forward elastostatic analyses

The forward elastostatic method for the direct stress determination in thin shells of arbitrary shape can also be implemented through finite-element analyses, in a procedure equivalent to the finite difference approach. In this alternative method, linear FE analyses are carried out on each known deformed configuration, in equilibrium with the external loads. Each deformed shape, which can change for every pressure value considered during the finite deformation of inflated thin shells, is imported in the finite-element software and subjected to the corresponding loading and boundary conditions. A linear analysis is run on each reconstructed and known geometry, assumed to be the reference state. Considering the independence of the stress state on the material stiffness, a fictitious unit elastic modulus is set, while Poisson's ratio is assumed the same as in the nonlinear FEA run to perform the validations. In this forward elastostatic FE method, carried out on reconstructed geometries and hence named here 'reconstructed FEA', only the stress field should be considered, while the displacements and strains, which depend on the material model, have to be treated as virtual.

The forward linear finite-element approach has been tested for the two problems considered in §§3a,b, respectively, and compared with the results presented therein. In the former validation, the deformed FE meshes from the finite inflation of a flat elliptical membrane with aspect ratio $b/a = 0.5$ are imported back in Abaqus and used as the reference configuration. Although the boundary conditions remain the same, the pressure and thickness field data change for each deformed state. The results from the 'reconstructed FEA' are shown in figure 12, where they are compared against the reference stresses from the large deformation FE inflation and finite difference results presented in figure 4. In all plots of figure 12, the reconstructed FE predictions agree very well with the reference results, thus proving the validity of the alternative finite-element forward elastostatic method.

In the second experimental validation, the DIC-extracted deformed shapes from TPU elliptic bulge tests were imported into Abaqus, along with pressure and thickness data. For each deformed configuration, an independent linear FE analysis was carried out to obtain the stress distribution. In this forward elastostatic FE analysis, the same grid spacing employed for the finite difference method was used to create the mesh using quadrilateral shell elements, for which the thickness h was prescribed from the nodal field data. Incompressible elastic properties with a fictitious unit modulus were assigned to the shell elements. The stresses from the reconstructed FEA are overlaid to the data obtained from nonlinear FEA and finite difference, figure 8*a*,*b*,

Downloaded from https://royalsocietypublishing.org/ on 14 December 2022

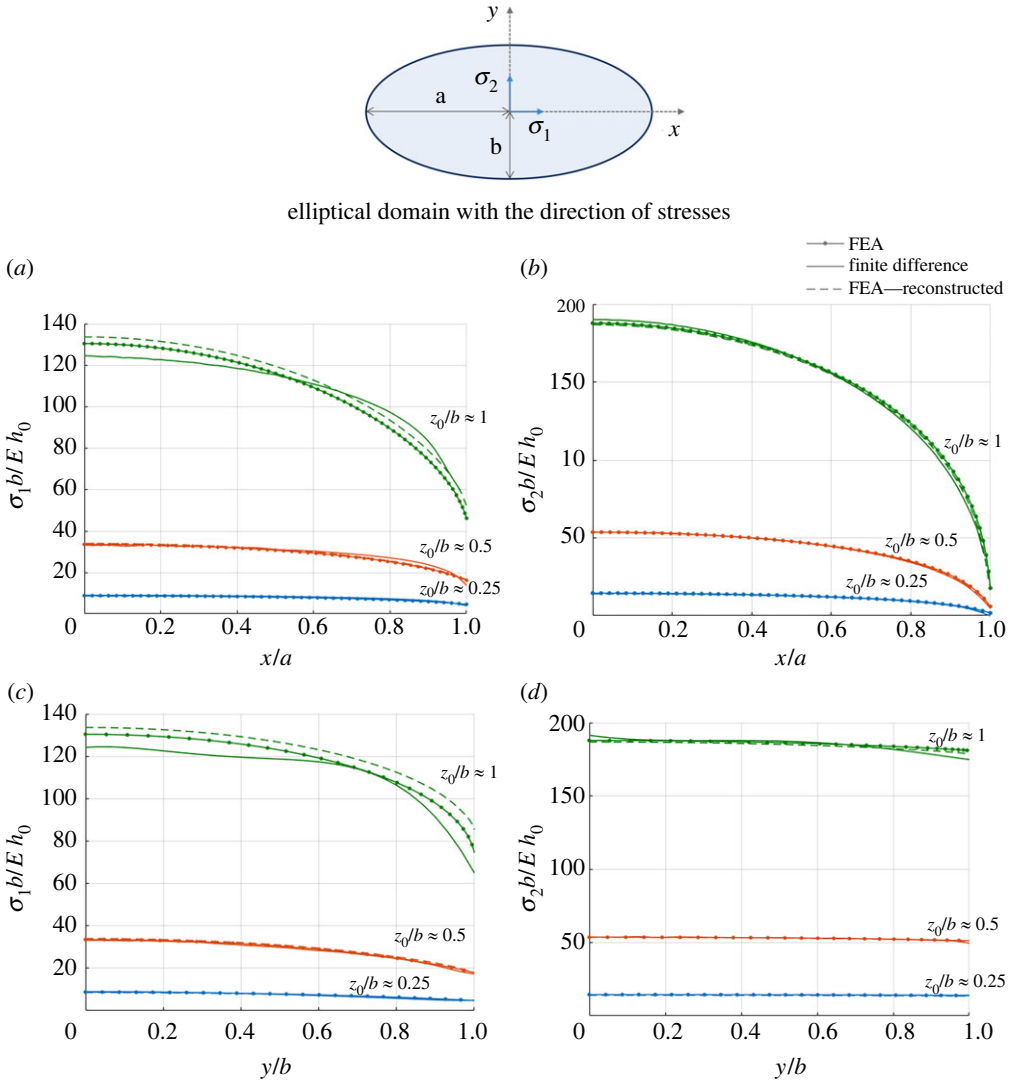

Figure 12. Normalized stress along the first principal direction, $\sigma_1 b/Eh_0$ (*a*,*c*), and second principal direction, $\sigma_2 b/Eh_0$ (*b*,*d*) plotted against the dimensionless coordinates x/a (*a*,*b*) and y/b (*c*,*d*) for $z_0/b \approx [0.25, 0.5, 1]$. The results from FE (solid line with dot), finite difference forward elastostatic method (solid line) and reconstructed FEA (dashed line) are compared for $\nu = 0.35$ during the inflation of planar elliptical shells with $b/a = 0.5$. (Online version in colour.)

and are presented in figure 13 for the three inflation tests performed on elliptical membranes with aspect ratio $b/a = 0.5$. Although the experimentally reconstructed FE results are overall in good agreement with the numerical predictions, they show more scattering than the finite difference data, obtained from the same experimental measurements. This is because the stress field is very sensitive to the deformed shape. Any inaccuracies or noise in the experimental surface fitting cause errors in the resulting stresses. For the finite difference code, the smoothed curvature data from DIC are directly employed in the computations, whereas, for reconstructed FEA, only the shell surface is given as an input, which cannot capture the local shape changes of the surface as curvature, proportional to the second derivative of the surface coordinates, does. Moreover, in figure 13*b*, one of the FE reconstructed results shows a higher deviation for σ_2 at high pressures, as the inflated shape from the DIC is not perfectly symmetric. By contrast, the smoothing of

Downloaded from https://royalsocietypublishing.org/ on 14 December 2022

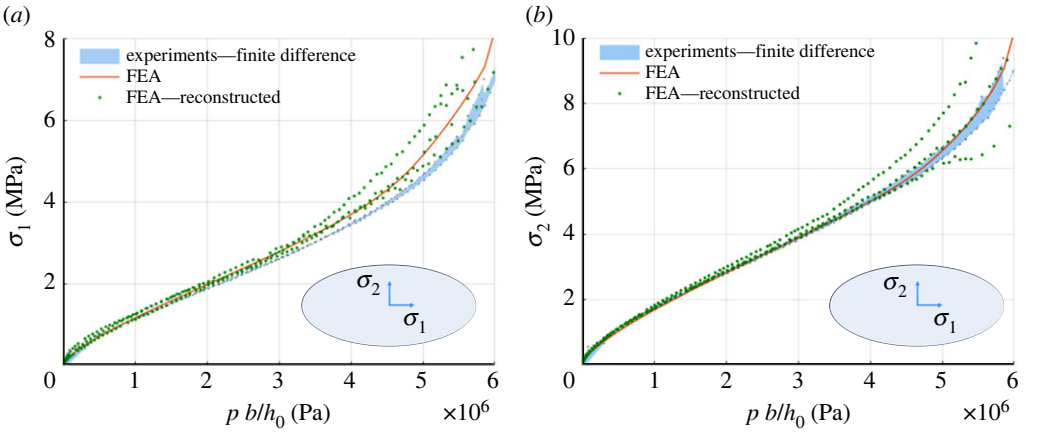

Figure 13. Comparison between the experimentally derived finite difference (blue region and dots) and FEA reconstructed (green dots) results, and FEA predictions from finite inflation (red curve) for the bulge test of elliptical TPU membranes of aspect ratio $b/a = 0.5$. The stresses in the first σ_1 (*a*) and second σ_2 (*b*) principal directions at the apex of the inflated thin shell are plotted against normalized pressure $p\,b/h_0$. (Online version in colour.)

the experimental curvatures from DIC in finite difference code forces the data to become more symmetric, thus reducing discrepancies in results for the finite difference formulation.

The finite-element forward elastostatic analysis was compared with the finite difference code for computational efficiency. Both methods took approximately the same time to compute the stresses for one deformed configuration. However, the finite difference code could be incorporated in the DIC software packages to provide the surface stresses along with kinematic quantities in real-time. Another benefit of the finite difference code lies in its flexibility to incorporate a spatial variation of stiffness or Poisson's ratio, as it would be required for elastoplastic analyses.

Appendix E. Linearization of the hyperelastic constitutive model

The polynomial form of the strain energy density function of degree m for an isotropic incompressible hyperelastic material is given by Rivlin & Saunders [54]

$$W(I_1, I_2) = \sum_{j=1}^{m} \sum_{i=1}^{m-j} P_{ij} (I_1 - 3)^i (I_2 - 3)^j, \tag{E 1}$$

where I_1 and I_2 are the invariants of the right Cauchy–Green strain tensor, while P_{ij} are the coefficient used to fit the response of TPU membranes, reported in table 1.

Consider a shell in a deformed state characterized by its strain energy density W_0. After reaching W_0, the shell is deformed again under small displacements. For an infinitesimal deformation identified by I_1' and I_2', the strain energy density function can be approximated by the first power of the polynomial strain energy density function, equation (E 1), as

$$W(I_1', I_2') = W_0 + P_{10}(I_1' - 3) + P_{01}(I_2' - 3), \tag{E 2}$$

where the last two terms coincide with the first-order Mooney–Rivlin model of a hyperelastic material, and they represent the tangent plane in the (I_1, I_2, W) space, as shown in figure 14. For small strains, the strain energy density $W(I_1', I_2')$ can be written as a function of the nominal strains,

Downloaded from https://royalsocietypublishing.org/ on 14 December 2022

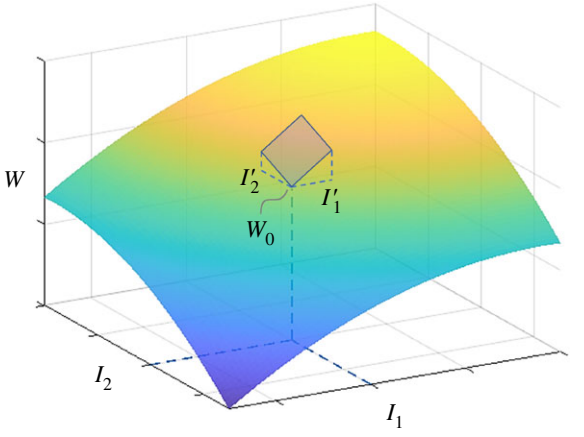

Figure 14. Tangent plane approximation (grey region) of a nonlinear strain energy density function for small deformation I_1' and I_2'. (Online version in colour.)

Table 1. Material parameters (in MPa) for the fifth-degree polynomial strain energy density function W for TPU, obtained by fitting uniaxial and equibiaxial stress–strain data.

coefficients	values	coefficients	values	coefficients	values	coefficients	values
P_{10}	1.372	P_{30}	−0.486	P_{31}	0.675	P_{41}	−0.071
P_{01}	1.745	P_{21}	0.596	P_{22}	−1.376	P_{32}	0.060
P_{20}	0.861	P_{12}	1.681	P_{13}	0.446	P_{23}	0.083
P_{11}	−3.363	P_{03}	−0.760	P_{04}	0.025	P_{14}	−0.064
P_{02}	0.720	P_{40}	−0.061	P_{50}	0.014	P_{05}	0.008

$W(\varepsilon_1, \varepsilon_2, \varepsilon_3)$. Denoting the principal stretches by U_i $(i = 1, 2, 3)$, the invariants are given by

$$I_1' = U_1^2 + U_2^2 + U_3^2$$
and
$$I_2' = U_1^2U_2^2 + U_2^2U_3^2 + U_3^2U_1^2. \tag{E 3}$$

Considering that $U = 1 + \varepsilon$ and the incompressibility condition is $\varepsilon_1 + \varepsilon_2 + \varepsilon_3 = 0$, the invariants can be written in the form of nominal strains as

$$I_1' = 3 + 2(\varepsilon_1^2 + \varepsilon_2^2 + \varepsilon_1\varepsilon_2)$$
and
$$I_2' = 3 + \varepsilon_1^4 + 2\varepsilon_1^3\varepsilon_2 + 6\varepsilon_1^2\varepsilon_2 + 6\varepsilon_1\varepsilon_2^2 + 3\varepsilon_1^2\varepsilon_2^2 + 2\varepsilon_1\varepsilon_2^3 + \varepsilon_2^4. \tag{E 4}$$

If high order powers of strains are neglected, equation (E 4) gives $I_2' \approx 3$. Hence, equation (E 2) becomes

$$W(\varepsilon_1, \varepsilon_2) = W_0 + 2P_{10}(\varepsilon_1^2 + \varepsilon_2^2 + \varepsilon_1\varepsilon_2), \tag{E 5}$$

from which the second Piola–Kirchhoff stress components can be obtained as $\sigma_i = \dfrac{\partial W}{\partial \varepsilon_i}$ by assuming that the Green–Lagrangian strain tensor is reduced to nominal strain for infinitesimal deformation

$$\sigma_1 = 2\,P_{10}(2\varepsilon_1 + \varepsilon_2)$$
and
$$\sigma_2 = 2\,P_{10}(2\varepsilon_2 + \varepsilon_1). \tag{E 6}$$

Equation (E 6) is similar to the linear elastic constitutive equations, equation (2.13), for an incompressible material. In particular, it should be noted that the coefficient P_{10} is a common

Downloaded from https://royalsocietypublishing.org/ on 14 December 2022

multiplicative factor, as it is the elastic modulus in equation (2.13). Therefore, if the former linearized constitutive relations are employed in equation (2.13), the solution for the stress distribution in the shell results independent of the hyperelastic material parameter P_{10}.

References

1. Zingoni A. 2018 *Shell structures in civil and mechanical engineering*, 2nd edn. London, UK: ICE Publishing.
2. Guest SD, Pellegrino S. 2006 Analytical models for bistable cylindrical shells. *Proc. R. Soc. A* **462**, 839–854. (doi:10.1098/rspa.2005.1598)
3. Moriello DS, Bosi F, Torii R, Tan PJ. 2020 Failure and detachment path of impulsively loaded plates. *Thin-Walled Struct.* **155**, 106871. (doi:10.1016/j.tws.2020.106871)
4. Adriaenssens S, Block P, Veenendaal D, Williams C. 2014 *Shell structures for architecture: form finding and optimization*. New York, NY: Routledge.
5. Lu J, Zhou X, Raghavan ML. 2008 Inverse method of stress analysis for cerebral aneurysms. *Biomech. Model. Mechanobiol.* **7**, 477–486. (doi:10.1007/s10237-007-0110-1)
6. Yu X, Fu Y, Dai HH. 2020 A refined dynamic finite-strain shell theory for incompressible hyperelastic materials: equations and two-dimensional shell virtual work principle. *Proc. R. Soc. A* **476**, 20200031. (doi:10.1098/rspa.2020.0031)
7. Arrieta AF, Kuder IK, Rist M, Waeber T, Ermanni P. 2014 Passive load alleviation aerofoil concept with variable stiffness multi-stable composites. *Compos. Struct.* **116**, 235–242. (doi:10.1016/j.compstruct.2014.05.016)
8. Bessa MA, Pellegrino S. 2018 Design of ultra-thin shell structures in the stochastic post-buckling range using Bayesian machine learning and optimization. *Int. J. Solids Struct.* **139**, 174–188. (doi:10.1016/j.ijsolstr.2018.01.035)
9. Gori M, Bosi F. 2022 Deployment and surface accuracy of regularly creased membranes. *Extreme Mech. Lett.* **56**, 101849. (doi:10.1016/j.eml.2022.101849)
10. Norman AD, Seffen KA, Guest SD. 2008 Multistable corrugated shells. *Proc. R. Soc. A* **464**, 1653–1672. (doi:10.1098/rspa.2007.0216)
11. Hutchinson JW. 2016 Buckling of spherical shells revisited. *Proc. R. Soc. A* **472**, 20160577. (doi:10.1098/rspa.2016.0577)
12. Bosi F, Schlothauer A, Leclerc C, Pellegrino S. 2018 Cure-induced deformation of ultra-thin composite laminates. In *AIAA/ASCE/AHS/ASC Structures, Structural Dynamics, and Materials Conference, FL, USA*, p. 2241.
13. Wang T, Yang Y, Xu F. 2022 Mechanics of tension-induced film wrinkling and restabilization: a review. *Proc. R. Soc. A* **478**, 20220149. (doi:10.1098/rspa.2022.0149)
14. Tay RTS, Sutera SP, Zahalak GI, Rao PR. 1987 Membrane stress and internal pressure in a red blood cell freely suspended in a shear flow. *Biophys. J.* **51**, 915–924. (doi:10.1016/S0006-3495(87)83419-7)
15. Kroon M, Holzapfel GA. 2008 Estimation of the distributions of anisotropic, elastic properties and wall stresses of saccular cerebral aneurysms by inverse analysis. *Proc. R. Soc. A.* **464**, 807–825. (doi:10.1098/rspa.2007.0332)
16. Genovese K, Casaletto L, Humphrey JD, Lu J. 2014 Digital image correlation-based point-wise inverse characterization of heterogeneous material properties of gallbladder in vitro. *Proc. R. Soc. A* **470**, 20140152. (doi:10.1098/rspa.2014.0152)
17. Marchand B, Chamoin L, Rey C. 2019 Parameter identification and model updating in the context of nonlinear mechanical behaviors using a unified formulation of the modified constitutive relation error concept. *Comput. Methods Appl. Mech. Eng.* **345**, 1094–1113. (doi:10.1016/j.cma.2018.09.008)
18. Zhou X, Raghavan ML, Harbaugh RE, Lu J. 2010 Patient-specific wall stress analysis in cerebral aneurysms using inverse shell model. *Ann. Biomed. Eng.* **38**, 478–489. (doi:10.1007/s10439-009-9839-2)
19. Beams JW. 1959 Mechanical properties of thin films of gold and silver. *Proceedings of an International Conference, Sponsored by Air Force Office of Scientific Research, Air Research and Development Command and The General Electric Research Laboratory*, pp. 183–192. NJ, USA: John Wiley and Sons, Inc.
20. Aguir H, BelHadjSalah H, Hambli R. 2011 Parameter identification of an elasto-plastic behaviour using artificial neural networks–genetic algorithm method. *Mater. Des.* **32**, 48–53. (doi:10.1016/j.matdes.2010.06.039)

Downloaded from https://royalsocietypublishing.org/ on 14 December 2022

21. Wang S, Guo Z, Zhou L, Li L, Fu Y. 2019 An experimental study of localized bulging in inflated cylindrical tubes guided by newly emerged analytical results. *J. Mech. Phys. Solids* **124**, 536–554. (doi:10.1016/j.jmps.2018.11.011)
22. Sutton MA, Orteu JJ, Schreier H. 2009 *Image correlation for shape, motion and deformation measurements: basic concepts, theory and applications*. New York, NY: Springer Science & Business Media.
23. Nguyen HN, Chamoin L, Minh CH. 2022 mcre-based parameter identification from full-field measurements: consistent framework, integrated version, and extension to nonlinear material behaviors. *Comput. Methods Appl. Mech. Eng.* **400**, 115461. (doi:10.1016/j.cma.2022.115461)
24. Ozdemir VB, Kwok K. 2022 Inflated cone experiment for high-throughput characterization of time-dependent polymer membranes. *J. Appl. Mech.* **89**, 074501. (doi:10.1115/1.4054523)
25. Bosi F, Pellegrino S. 2017 Molecular based temperature and strain rate dependent yield criterion for anisotropic elastomeric thin films. *Polymer* **125**, 144–153. (doi:10.1016/j.polymer.2017.07.080)
26. Bosi F, Pellegrino S. 2018 Nonlinear thermomechanical response and constitutive modeling of viscoelastic polyethylene membranes. *Mech. Mater.* **117**, 9–21. (doi:10.1016/j.mechmat.2017.10.004)
27. Mitchell JS, Zorman CA, Kicher T, Roy S, Mehregany M. 2013 Examination of bulge test for determining residual stress, Young's Modulus, and Poisson's Ratio of 3C-SiC thin films. *J. Aerosp. Eng.* **16**, 46–54. (doi:10.1061/(ASCE)0893-1321(2003)16:2(46))
28. Karimi A, Shojaei OR, Kruml T, Martin JL. 1997 Characterisation of tin thin films using the bulge test and the nanoindentation technique. *Thin Solid Films* **308**, 334–339. (doi:10.1016/S0040-6090(97)00566-X)
29. Edwards RL, Coles G, Sharpe WN. 2004 Comparison of tensile and bulge tests for thin-film silicon nitride. *Soc. Exp. Mech.* **44**, 49–54. (doi:10.1007/BF02427976)
30. Kalkman AJ, Verbruggen AH, M. Janssen GCA, Groen FH. 1999 A novel bulge-testing setup for rectangular free-standing thin films. *Rev. Sci. Instrum.* **70**, 4026–4031. (doi:10.1063/1.1150029)
31. Yousif MI, Ducan JL, Johnson W. 1970 Plastic deformation and failure of thin elliptical diaphragms. *Int. J. Mech. Sci.* **12**, 959–972. (doi:10.1016/0020-7403(70)90036-6)
32. Machado G, Favier D, Chagnon AG. 2012 Membrane curvatures and stress-strain full fields of axisymmetric bulge tests from 3D-DIC measurements. Theory and Validation on virtual and experimental results. *Exp. Mech.* **52**, 865–880. (doi:10.1007/s11340-011-9571-3)
33. Hill R. 1950 A theory of the plastic bulging of a metal diaphragm by lateral pressure. *Lond. Edinb. Dublin Philos. Mag. J. Sci.* **41**, 1133–1142. (doi:10.1080/14786445008561154)
34. Vlassak JJ, Nix WD. 1992 A new bulge test technique for the determination of Young's modulus and Poisson's ratio of thin films. *J. Mater. Res.* **7**, 3242–3249. (doi:10.1557/JMR.1992.3242)
35. Neggers J, Hoenagels J, Hild F, Roux S, Geers M. 2014 Direct stress-strain measurements from bulged membranes using topography image correlation. *Exp. Mech.* **54**, 717–727. (doi:10.1007/s11340-013-9832-4)
36. Khayat RE, Derdouri A. 1995 Stretch and inflation of hyperelastic membranes as applied to blow molding. *Polym. Eng. Sci.* **35**, 1852–1863. (doi:10.1002/pen.760352304)
37. Khayat RE, Derdouri A. 1994 Inflation of hyperelastic cylindrical membranes as applied to blow moulding. Part II. Non-Axisymmetric Case. *Int. J. Numer. Methods Eng.* **37**, 3793–3808. (doi:10.1002/nme.1620372204)
38. Verron E, Marckmann G, Peseux B. 2001 Dynamic inflation of non-linear elastic and viscoelastic rubberlike membranes. *Int. J. Numer. Methods Eng.* **50**, 1233–1251. (doi:10.1002/1097-0207(20010220)50:5<1233::AID-NME77>3.0.CO;2-W)
39. Jayyosi C, Garnier KB, Coret M. 2017 Geometry of an inflated membrane in elliptic bulge tests: evaluation of an ellipsoidal shape approximation by stereoscopic digital image correlation measurements. *Med. Eng. Phys.* **48**, 150–157. (doi:10.1016/j.medengphy.2017.06.020)
40. Tonge TK, Atlan LS, Voo LM, Nguyen TD. 2013 Full-field bulge test for planar anisotropic tissues: part I – experimental methods applied to human skin tissue. *Acta Biomater.* **9**, 5913–5925. (doi:10.1016/j.actbio.2012.11.035)
41. Tonge TK, Voo LM, Nguyen TD. 2013 Full-field bulge test for planar anisotropic tissues: part II – a thin shell method for determining material parameters and comparison of two distributed fiber modeling approaches. *Acta Biomater.* **9**, 5926–5942. (doi:10.1016/j.actbio.2012.11.034)

42. Govindjee S, Mihalic PA. 1996 Computational methods for inverse finite elastostatics. *Comput. Methods Appl. Mech. Eng.* **136**, 47–57. (doi:10.1016/0045-7825(96)01045-6)
43. Foster HO. 1967 Very large deformation of axially symmetrical membranes made of neo-hookean materials. *Int. J. Eng. Sci.* **5**, 95–117. (doi:10.1016/0020-7225(67)90056-0)
44. Green AE, Zerna W. 1968 *Theoretical elasticity*, 2nd edn. London, UK: Oxford University Press.
45. Ventsel E, Krauthammer T. 2001 *Thin plates and shells, theory, analysis, and applications*, 1st edn. New York, NY: Marcel Dekker Inc.
46. Goldstein H, Poole C, Safko J. 2002 *Classical mechanics*, 3rd edn. Boston, MA: Addison Wesley.
47. Novozhilov VV. 1964 *Thin shell theory* (translated from the second Russian edition by P. G. Lowe; edited by J. R. M. Radok.), 2nd edn. Groningen, the Netherlands: P. Noordhoff.
48. Flugge W. 1973 *Stresses in shells*, 2nd edn. Heidelberg, Berlin, Germany: Springer.
49. Edmondson AJ. 1970 Solution of shell problems by finite difference method. *Nucl. Eng. Des.* **11**, 208–216. (doi:10.1016/0029-5493(70)90144-5)
50. Sheng JY, Zhang LY, Li B, Wang GF, Feng XQ. 2017 Bulge test method for measuring the hyperelastic parameters of soft membranes. *Acta Mech.* **228**, 4187–4197. (doi:10.1007/s00707-017-1945-x)
51. Fichter WB. 1997 Some solutions for the large deflection of uniformly loaded circular membranes. Technical report, NASA Langley Research Center; Hampton, VA United States.
52. Bigoni D, Bosi F, Misseroni D, Dal Corso F, Noselli G. 2015 New phenomena in nonlinear elastic structures: from tensile buckling to configurational forces. In *Extremely deformable structures*, pp. 55–135. Vienna, Austria: Springer.
53. Mihai LA, Goriely A. 2017 How to characterize a nonlinear elastic material? A review on nonlinear constitutive parameters in isotropic finite elasticity. *Proc. R. Soc. A* **473**, 20170607. (doi:10.1098/rspa.2017.0607)
54. Rivlin RS, Saunders DW. 1951 Large elastic deformations of isotropic materials VII. Experiments on the deformation of rubber. *Phil. Trans. R. Soc. Lond. A* **243**, 251–288. (doi:10.1098/rsta.1951.0004)

Downloaded from https://royalsocietypublishing.org/ on 14 December 2022